

REVIEWS OF TOPICAL PROBLEMS PACS numbers: **05.45.** – **a**, **47.52.** + **j**, **92.10.** – **c**

Chaotic advection in the ocean

K V Koshel, S V Prants

DOI: 10.1070/PU2006v049n11ABEH006066

Contents

Abstract. The problem of chaotic advection of passive scalars in the ocean and its topological, dynamical, and fractal properties are considered from the standpoint of the theory of dynamical systems. Analytic and numerical results on Lagrangian transport and mixing in kinematic and dynamic chaotic advection models are described for meandering jet currents, topographical eddies in a barotropic ocean, and a two-layer baroclinic ocean. Laboratory experiments on hydrodynamic flows in rotating tanks as an imitation of geophysical chaotic advection are described. Perspectives of a dynamical system approach in physical oceanography are discussed.

1. Introduction

In the last decade, methods of the theory of dynamical systems were actively used in physical oceanography to describe the transport and mixing of water masses (together with salinity, heat, nutrients, pollutants, and other tracers) by coherent structures in the ocean [1 – 4]. Coherent structures are stable meso- and submesoscale features with a lifetime exceeding all Eulerian temporal characteristics. A modern technique for visualizing ocean flows with the help of neutrally buoyant floats, drifters, and radars can reveal various Eulerian coherent structures: planetary gyres, mesoscale and smaller size eddies, jets, and filaments. In Fig. 1, we show a satellite image of the Gulf Stream (for April 17, 1989) from the NOAA-N advanced high-resolution radiometer (the USA National Oceanic and Atmospheric Administration) [5]. The strong meandering jet current divides the warm saline water of the Sargasso sea and cool fresh Slope Water. A loop of the meander is seen in the figure.

This review is devoted to the transport, mixing, and chaotic advection in geophysical flows. If advected particles are small enough, rapidly adjust their own velocity to that of

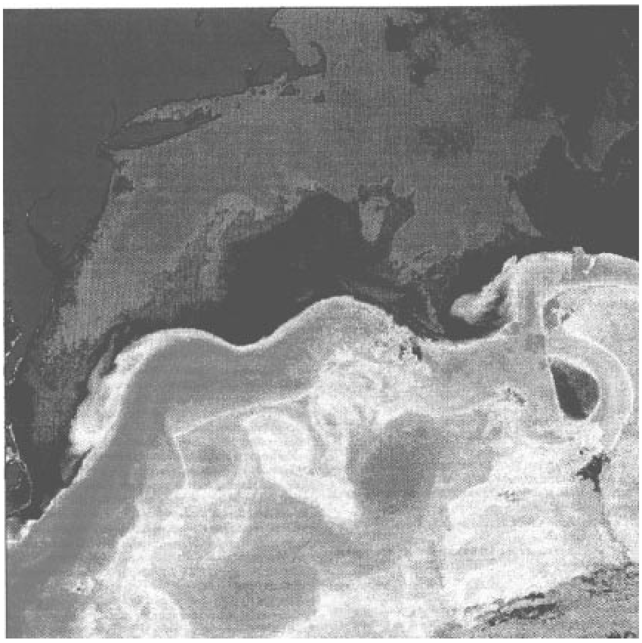

Figure 1. Satellite image of the Gulf Stream for April 17, 1989. Data are from the NOAA-N advanced high-resolution radiometer.

K V Koshel, S V Prants Il'ichev Pacific Oceanological Institute,
Far-Eastern Branch of the Russian Academy of Sciences,
ul. Baltiiskaya 43, 690041 Vladivostok, Russian Federation
Tel. (7-4232) 312-860, (7-4232) 316-419, (7-4232) 312-602
Fax (7-4232) 312-573
E-mail: kvkoshel@poi.dvo.ru, prants@poi.dvo.ru

Received 17 February 2006
Uspekhi Fizicheskikh Nauk **176** (11) 1177 – 1206 (2006)
Translated by S V Prants; edited by A M Semikhatov

the ambient flow (i.e., the inertial effects are negligibly small), and do not affect the flow properties, then the advection is called passive, and the particles are called passive (scalars, tracers, or Lagrangian particles). The equation of motion for such a passive particle is very simple,

$$\frac{\mathrm{d}\mathbf{r}}{\mathrm{d}t} = \mathbf{v}(\mathbf{r}, t), \tag{1}$$

where $\mathbf{r} = (x, y, z)$ and $\mathbf{v} = (u, v, w)$ are the position vector and the particle velocity at a point with coordinates (x, y, z). The Eulerian velocity field is supposed to be known as a result of solving dynamical equations of motion (the dynamical approach) or due to some kinematical speculations or measurements. The dynamics of tracers are described in nontrivial cases by the set of nonlinear differential equations (1) with fully deterministic right-hand sides (the Eulerian velocity field being regular), whose phase space is the physical space of advected particles. It is well known from the theory of dynamical systems that solutions of deterministic equations can be chaotic in the sense of the exponential sensitivity to small variations in initial conditions and/or parameters. Dynamical chaos is not an exotic phenomenon; chaos occurs even in very simple systems and has been observed in numerous laboratory experiments. The geometric structures, called invariant manifolds, that determine motion in the phase space have been well studied in the theory of nonlinear dynamical systems, at least in low-dimensional ones. Examples of the invariant manifolds are stationary points, attractors (including strange ones), invariant tori, Cantor tori, and stable and unstable manifolds (see the vast literature on chaos theory in dynamical systems, for example, Refs [6–8]). In hydrodynamics, it is natural to call such coherent structures Lagrangian. The Lagrangian structures determine global mixing in fluids. In real fluids, molecular diffusion and multi-scale turbulence must also be taken into account. The Lagrangian structures consist of fluid particles and are not visible on maps of nonstationary currents measured by some means or other. In laboratory experiments, they can be visualized with the help of dye. In the ocean, we can obtain information about them using drifters and neutrally buoyant floats. The theory of dynamical systems is able to suggest where and when floats should be launched, to give us maximum information about a flow under consideration with a minimum number of floats.

The main task in theoretical physical oceanography is to simulate Eulerian velocity fields, typically by means of numerical integration of relatively complicated dynamically consistent models. Velocity fields in nontrivial models of ocean basins and in the real ocean vary within wide spatial and temporal ranges. By solving advection equations (1) for passive particles, it is possible to obtain valuable information about Lagrangian coherent structures determining barriers to transport, exit channels, and regions of intensive mixing and stagnation.

In Section 2, we provide general information about the transport, mixing, and chaotic advection of passive particles in hydrodynamic flows. A picture of an arising stochastic layer, which is a 'seed' of Hamiltonian chaos, is presented. In Section 3, we describe the simplest kinematic model for chaotic advection, which contains the main Eulerian structures, a vortex and a background current with a periodic component. This model illustrates the general scenario of arising chaotic advection and its topological, dynamical, and fractal properties, which are typical of all kinematic and dynamical models for this phenomenon in the ocean. In Section 4, we briefly review kinematic models of chaotic advection in meandering jet currents, like the Gulf Stream and the Kuroshio, and in planetary gyres. In Section 5, we review chaotic advection in a number of dynamical models built on the basic of the concept of background currents developed by V F Kozlov. We present the results of simulation of Lagrangian transport and mixing in the barotropic model with a semicircular basin having a source and a sink and in the models with topographical vortices, a background flow, and a tidal current. The simple two-layer model of a baroclinic ocean and the efficiency of chaotic mixing depending on a perturbation frequency are discussed in that section. The experimental models of Eulerian coherent structures in the ocean — jet currents, eddies, Rossby waves, and their interaction — have been created in a number of laboratories in the world. In Section 6, we describe laboratory experiments on hydrodynamic flows in rotating tanks as an imitation of the interaction between a periodic flow and two gyres and a geostrophic jet with Rossby waves. Perspectives of a dynamical system approach in physical oceanography are discussed in the concluding section.

We dedicate the present review to the memory of Vadim Fedorovich Kozlov, the outstanding scientist who made an important contribution to physical oceanography and, in particular, to the theory of chaotic advection in the ocean.

2. Transport, mixing, and advection

The term 'transport' means the motion of fluid particles from one spatial region to another. In the theory of dynamical systems, it is the phase-space motion of points representing a dynamical system with different initial conditions. The quantitative measures of transport are the flux of a fluid through a fixed surface and the spatial extent determined by the size of the particle distribution. Under certain conditions, material surfaces arise in a fluid, filled up by trajectories of fluid particles. Trajectories of fluid particles cannot traverse these surfaces, which are therefore barriers to transport. For example, the so-called Kolmogorov–Arnold–Moser (KAM) tori (or KAM tubes of flow) [7–9] are absolute barriers to transport. On the other hand, there are so-called accelerator modes [8] that enhance transport.

Mixing, which is a key concept in both hydrodynamics and the theory of dynamical systems, is defined in a rigorous mathematical sense. We consider a basin A with a circulation, containing a domain B with a contaminant occupying the volume $V(\mathrm{B}_0)$ at $t = 0$. We consider a domain C in A. The volume of the contaminant in the domain C at time t is $V(\mathrm{B}_t \bigcap \mathrm{C})$, and its concentration in C is given by the ratio of volumes $V(\mathrm{B}_t \bigcap \mathrm{C})/V(\mathrm{C})$. The definition of mixing is that for any domain C in A, we have the same concentration of the contaminant as for the entire domain A, i.e., $V(\mathrm{B}_t \bigcap \mathrm{C})/V(\mathrm{C}) - V(\mathrm{B}_0)/V(\mathrm{A}) \to 0$ as $t \to \infty$. It is the definition of global mixing. The mixing is determined not by an instantaneous field of passive scalars but by its evolution. In the theory of dynamical systems, the global mixing means a process of deformation of a small phase-space volume into a long intricate filament occupying all the energetically accessible domain of the phase space. The mixing measures are Lyapunov exponents. In geophysical flows, mixing due to flow kinematics is complicated by the accompanying molecular diffusion and multi-scale turbulence.

2.1 Chaotic advection

We consider the vector equation for advection of passive scalars (1). If $\mathbf{v}$ is a nonlinear function of the particle position $\mathbf{r}$, then, as is known from the theory of dynamical systems, chaotic solutions of Eqn (1) are possible even if the Eulerian velocity field is deterministic and smooth. Deterministic or dynamical chaos is defined rigorously in the theory and in fact means extreme sensitivity to small variations in the initial conditions $|\delta\mathbf{r}(0)|$. This means that $|\delta\mathbf{r}(t)|$ increases exponentially in the course of time with almost any choice of $\delta\mathbf{r}(0)$,

$$|\delta\mathbf{r}(t)| = |\delta\mathbf{r}(0)| \exp(\lambda t) , \tag{2}$$

where λ is a positive coefficient known as a Lyapunov exponent and $|\ldots|$ is the norm of a vector. The exact direction of the vector $\delta\mathbf{r}(0)$ does not matter because most of these vectors (in the sense of zero measure) evolve in the direction of maximum stretching of the corresponding fluid volume. The exponent λ asymptotically (as $t \to \infty$) characterizes the mean velocity of such a stretching. If the fluid is incompressible ($\operatorname{div}\mathbf{v} = 0$), the volume shrinks along another direction with the same mean velocity but of the opposite sign. There is a third direction in three-dimensional Hamiltonian flows, along which the velocity of stretching (shrinking) is zero. In other words, the sum of all the Lyapunov exponents in a Hamiltonian system is zero. Equation (2) implies a fact that is important from the practical standpoint — chaos limits a forecast even for simple nonlinear systems by a prognosis time of the order of

$$\tau_{\mathrm{p}} \approx \frac{1}{\lambda} \ln \frac{\Delta a}{\Delta a(0)} , \tag{3}$$

where Δa is the confidence interval for forecasting a given dynamical variable a and $\Delta a(0)$ is the practically inevitable error in measuring its initial value. Trajectories that diverge exponentially in a short time in a bounded phase space of a dynamical system return (at least, in Hamiltonian systems) to their initial points (the Poincaré theorem on recurrences). Because the phase space is a physical space for two-dimensional advection problems, this property, known as chaotic mixing, is very important for oceanic flows. Chaotic mixing in fluids is called 'chaotic advection' [10, 11] (the term 'Lagrangian turbulence' is sometimes used).

The theory of dynamical systems implies that Eqn (1) for a steady plane flow (it does not matter how complicated it is) is integrable, trajectories of fluid particles coincide with streamlines Ψ, and material lines stretch (if they stretch at all) in direct proportion to time t. Even a simple perturbation of a planar flow (periodic or quasi-periodic) may cause cardinal changes: mixing, exponential stretching of material lines in the course of time, chaos, and so on. In general, three-dimensional steady flows cannot be written in a Hamiltonian form, which does not prevent them from being chaotic. Moreover, V I Arnold was the first to suggest chaos in the field lines and, therefore, in trajectories, for a special class of three-dimensional stationary flows (so-called ABC flows) [12, 13]. The important role of mixing in geophysical flows was stressed by Eckart [14] and Welander [15] more than 50 years ago. In paper [15], the ideas of fractal geometry have been used (without mention of the term) to explain how the length of an advected material line tends to infinity in spite of a finite area of closing.

The velocity components of incompressible planar flows are known [16] to be expressed in terms of a streamfunction:

$$u = -\frac{\partial\Psi}{\partial y} , \qquad v = \frac{\partial\Psi}{\partial x} . \tag{4}$$

Advection equations (1) are now the Hamiltonian equations

$$\frac{\mathrm{d}x}{\mathrm{d}t} = -\frac{\partial\Psi}{\partial y} , \qquad \frac{\mathrm{d}y}{\mathrm{d}t} = \frac{\partial\Psi}{\partial x} \tag{5}$$

with the streamfunction $\Psi(x, y, t)$ playing the role of a Hamiltonian. The particle coordinates x and y on the plane are canonically conjugate variables and the phase space of Eqn (5) is a configuration space. Thus, two-dimensional advection in an incompressible fluid is equivalent to the Hamiltonian dynamics of a system with one and a half degrees of freedom in the nonstationary case and with one degree of freedom in the stationary one. The Hamiltonian character of advection follows from the incompressibility condition and is also valid for viscous two-dimensional flows.

2.2 Stochastic layer

As was first found by Poincaré [17], a separatrix splitting may occur in Hamiltonian systems under an arbitrarily small perturbation. The splitting is an obstruction to the integrability of the perturbed system under consideration. Moreover, stable and unstable manifolds of a saddle point (which lies on the unperturbed separatrix) intersect transversely and, as a consequence, a stochastic layer appears near the unperturbed separatrix. The occurrence of a stochastic layer in nonintegrable Hamiltonian systems is a universal phenomenon. Just this layer is a 'seed' of chaos. The instability of motion near the unperturbed separatrix has the following simple reason: the frequency of oscillations or rotations of particles far away from the unperturbed separatrix depends weakly on energy (action), and its small variations result in small variations in phase for the period of oscillations. The period of oscillations near the unperturbed separatrix tends to infinity, and small variations in frequency there may cause large changes in phase. This is the reason for a local instability of trajectories in a stochastic layer. Motion there is very intricate, and many problems are far from being solved, despite the extensive efforts (see a review of the results in Ref. [8]).

Following Ref. [18], we present a visual Poincaré's proof of splitting and intersection of stable and unstable manifolds in the homoclinic case, i.e., with a single saddle point. The phase portrait of the unperturbed system is given by a separatrix loop intersecting itself at the saddle point and separating finite (inside the loop) and infinite (outside it) trajectories (Fig. 2a). A specific example of such a flow is given in Section 3. Let $\Psi^{(\pm)}$ be the lines of intersection of stable and unstable manifolds of the saddle point with the plane $\tau = 0$. We first suppose that they do not intersect each other under a sufficiently small perturbation and there is a small gap Δ between those lines (Fig. 2b). Under the map by the period T, the segment Δ shifts counter-clockwise. Because $\Psi^{(\pm)}$ are invariant under such a map, the domain D limited by the curves $\Psi^{(\pm)}$ and the segment Δ must occupy its proper

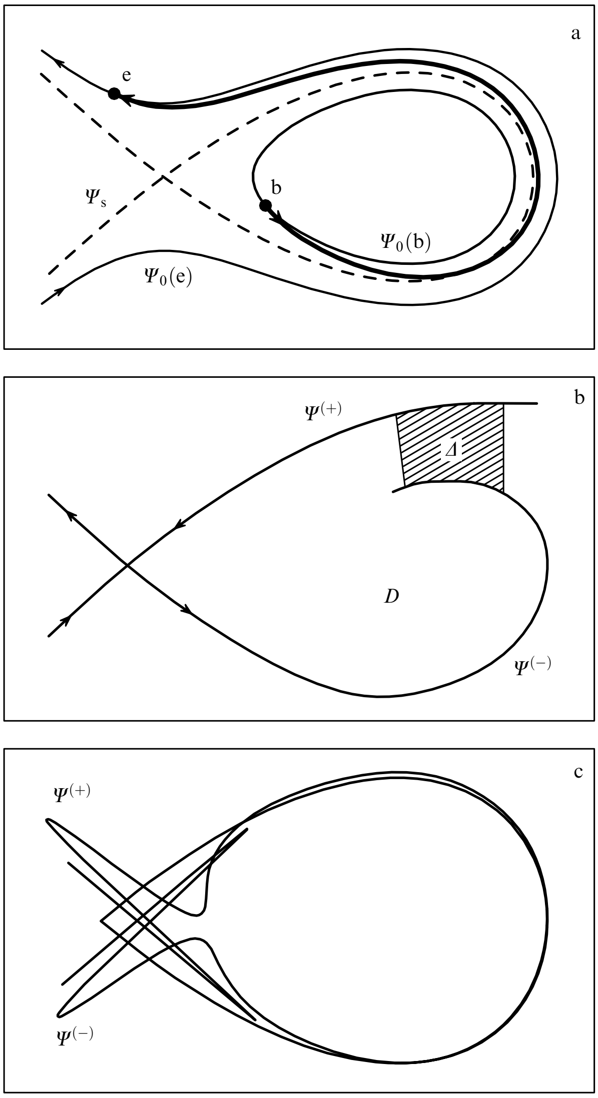

Figure 2. Emergence of a stochastic layer: (a) the loop of the unperturbed separatrix with the streamfunction Ψ_s, unperturbed trajectories (thin solid lines) of particles inside and outside the loop with the streamfunctions $\Psi_0(\mathrm{b})$ and $\Psi_0(\mathrm{e})$, respectively, and the particle trajectory under perturbation (thick curve); (b) splitting of the stable $\Psi^{(+)}$ and unstable $\Psi^{(-)}$ manifolds of the saddle point; (c) transverse intersections of the manifolds.

subdomain (the area D minus the shadowed area). But this contradicts the equality of the phase space volumes in Hamiltonian systems under the map $V(D) = V(\hat{T}(D))$. The contradiction is resolved if $\Psi^{(+)}$ and $\Psi^{(-)}$ intersect each other as shown schematically in Fig. 2c.

Separatrix splitting gives rise to important consequences for geophysical flows because it breaks down impermeable barriers and allows transporting tracers between domains not communicating in the unperturbed flow. The estimates of instant and mean fluxes between those domains and the exchange rates can be given with the help of the so-called Melnikov integral [19], which characterizes the instantaneous distance between the splitting separatrices Δ and the stochastic layer width. In the absence of perturbation, particles move along the streamlines Ψ_0 (thin solid lines in Fig. 2a). Under perturbation with a streamfunction $\Psi_1(\tau)$, particle b, placed at $\tau = 0$ on the streamline $\Psi_0(\mathrm{b})$ inside the separatrix loop, moves for a time τ to position e corresponding to another streamline $\Psi_0(\mathrm{e})$ (Fig. 2a). To compute the difference between the two unperturbed streamlines $\Delta\Psi_0 = \Psi_0(\mathrm{e}) - \Psi_0(\mathrm{b})$, we need to compute the derivative

$$\frac{\mathrm{d}\Psi\big(x(\tau), y(\tau)\big)}{\mathrm{d}\tau} = \frac{\partial\Psi_1}{\partial x}\frac{\partial\Psi_0}{\partial y} - \frac{\partial\Psi_1}{\partial y}\frac{\partial\Psi_0}{\partial x} \equiv \{\Psi_1, \Psi_0\}, \quad (6)$$

which is found with the help of advection equations (5) and the definition of the Poisson bracket $\{\Psi_1, \Psi_0\}$. It follows from Eqn (6) that for trajectories near the unperturbed separatrix (x_s, y_s), with an accuracy up to the first order of smallness in the perturbation strength ξ, this difference is

$$\Delta\Psi_0(\tau_0) = \int_{-\infty}^{\infty} \Big\{\Psi_1\big[x_s(\tau-\tau_0),\, y_s(\tau-\tau_0)\big],\; \Psi_0\big[x_s(\tau-\tau_0),\, y_s(\tau-\tau_0)\big]\Big\}\,\mathrm{d}\tau, \quad (7)$$

where the parameter τ_0 is introduced to take a perturbation phase into account. Using Eqn (7), the change of variable $\tau \to \tau' + \tau_0$, and trigonometric equalities, we find

$$\Delta\Psi_0(\tau_0) = \xi M_0 \sin\delta, \quad (8)$$

where the Melnikov integral M_0 and the phase δ are calculated by integrating Eqn (7) over τ'. The width of the stochastic layer is estimated as

$$\Delta = \frac{2\xi}{\pi}\frac{|M_0|}{|u_0|}, \quad (9)$$

where u_0 is the horizontal particle velocity. Thus, the flux $F = u_0\Delta$ is

$$F = \frac{2\xi}{\pi}|M_0|. \quad (10)$$

It is the same expression as the one obtained using the area of lobes in a homo- or heteroclinic structure [20].

In typical Hamiltonian systems, mixing is not homogeneous [8, 21]. For two-dimensional chaotic advection, this means that there are spatial domains (so-called islands) where fluid motion is regular. Normally, there is a hierarchy of islands: large islands are surrounded by chains of small ones, which are in turn surrounded by smaller ones, and so on, up to infinity (in theory). The islands are imbedded in the chaotic sea where the motion of fluid elements (or passive scalars) is not regular. Particles cannot go through the island boundaries from either inside or outside; in other words, those boundaries are barriers to particle transport. There are so-called sticky zones near the outer boundaries of the islands where particles can be trapped for a long time. Sticking may strongly change the statistical properties of transport. For example, the variance of particle displacements increases not as t (the case of normal diffusion) but as t^{μ}, where the so-called transport exponent μ can be less than unity (subdiffusion) or greater than unity (superdiffusion). All these dynamical characteristics of chaotic advection are determined by specific geometric structures (the invariant manifold), to be illustrated in Section 3 with a simple kinematical model.

3. Basic model for chaotic advection

In this section, in the geometric approach framework, we describe the mixing of passive scalars in a flow consisting of the main Eulerian coherent structures: an unsteady current and a vortex. A planar flow of ideal fluid with the given streamfunction is considered [22]:

$$\Psi(\tau) = \ln\sqrt{x^2 + y^2} + \varepsilon x + \Psi_1(\tau)\,, \tag{11}$$

where the first term in the right-hand side represents a point-like vortex placed at the origin of the Cartesian plane x, y, the second term describes a spatially homogeneous meridional flow, i.e., a steady current along the y axis from the south to the north with the dimensionless velocity ε, and $\Psi_1(\tau)$ is a nonstationary streamfunction, which is chosen to have the simple form $\Psi_1(\tau) = \xi x \sin \nu\tau$.

Advection equations for passive scalars are written in Hamiltonian form (5) as

$$\begin{aligned} \dot{x} &= -\frac{y}{x^2 + y^2}\,, \\ \dot{y} &= \frac{x}{x^2 + y^2} + \varepsilon + \xi \sin \nu\tau\,, \end{aligned} \tag{12}$$

where the dot denotes the derivative with respect to the normalized time τ. In the absence of perturbation ($\xi = 0$), the phase portrait of the system is given by a collection of finite and infinite trajectories separated by a loop passing through a saddle point with the coordinates $x = -1/\varepsilon$, $y = 0$. Depending on initial positions, particles either move inside the separatrix loop along closed streamlines or round the loop and move along infinite streamlines (Fig. 2a). It was shown analytically in Ref. [22] that an arbitrarily small perturbation splits the separatrix and gives rise to transverse intersections of stable and unstable manifolds of the saddle point, shown schematically in Fig. 2c, and to a homoclinic structure with an infinite variety of periodic and aperiodic orbits. The trajectories of passive scalars deviate from the steady-flow streamlines. We define the free-stream region (with incoming and outgoing components), the mixing region, and the vortex core as the respective sets of trajectories for which the number of times they wind around the vortex is zero, finite, and infinite. The Melnikov integral

$$M(\tau_0) = \int_{-\infty}^{\infty} u\big[x_s(\tau - \tau_0),\, y_s(\tau - \tau_0)\big] \cos(\nu\tau + \delta)\, d\tau \tag{13}$$

estimates an instant flux through the gap Δ between the splitting manifolds at the time τ_0 (Fig. 2b). The integral depends on the perturbation frequency ν and the phase of the meridional flow δ.

The phase-space topology depends strongly on the values of the control parameters ε and ξ because they are defined in terms of the velocity of the steady flow, unsteady-flow frequency, and vortex strength that determines the particle rotation frequency. Their relative values determine the orders of nonlinear resonances in the system. As the value of ε/ξ increases, the vortex core (occupied mainly by regular trajectories) grows and the orders of surviving resonances increase while the mixing region shrinks correspondingly. When $\varepsilon/\xi \gg 1$, the dynamics of the system are almost regular. Numerical simulation was performed for $\varepsilon = 0.5$, $\xi = 0.1$, and $\nu = 1$, in which case the mixing region is abundant with various topological structures.

3.1 Invariant sets of the flow

The invariant sets of dynamical system (12), which are the building blocks of its structure, have been described in Ref. [23]. Particles belonging to different sets exhibit qualitatively different behavior. The trivial examples of invariant sets are the entire phase space, a fixed point, a closed trajectory, and any trajectory defined over the time interval from $-\infty$ to ∞. We exclude the set of trajectories not winding around a vortex from the present analysis. We first consider the set of invariant curves filling up the KAM tori, the set of all periodic and quasi-periodic trajectories of passive scalars around the vortex center. In the Poincaré cross section (a collection of coordinates of particles with different initial conditions marked by points on the flow plane at times that are integer multiples of the period), they make up families of nested closed smooth curves (Fig. 3). Most of them lie inside the vortex core. Other families of invariant curves make up stability islands centered at elliptic points, which are located both in the vortex core and in the mixing region. The islands arise due to nonlinear resonances of various orders between particle motion around the vortex and the 2π-periodic perturbation. Under a high resolution, one can see the chains of the islands in the vortex core, which are surrounded by narrow stochastic layers. The vortex core is preserved for any values of the flow parameters ε and ξ. In other words, it is a robust structure. Because the frequency

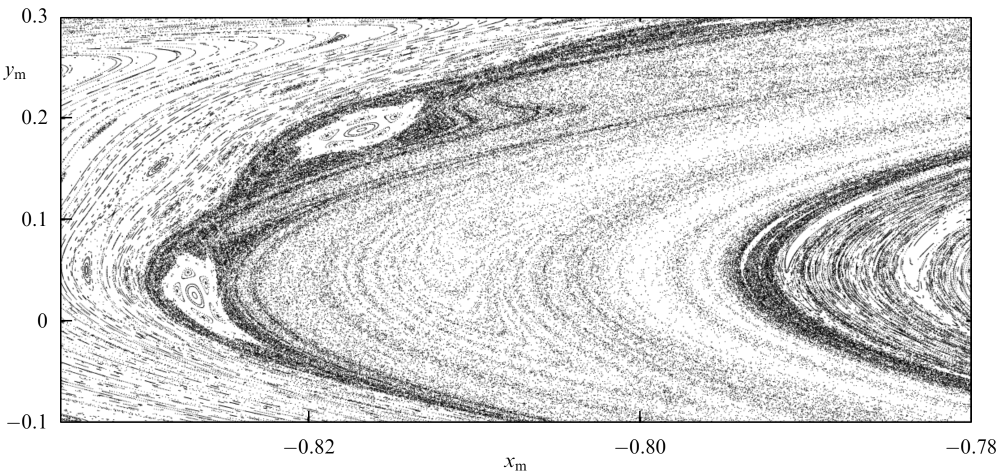

Figure 3. The plane of the Poincaré cross section of flow (11).

of particle rotations in the vortex core is much higher than the perturbation frequency, the perturbation can be considered adiabatic with respect to most orbits inside the core and the orbits can be considered regular, except for trajectories near the overlapping higher-order resonances, which make up very narrow stochastic layers. Being absolutely impermeable barriers, the KAM tori limit transport and mixing of passive scalars.

Perturbation gives rise to cantori replacing some KAM tori, first of all, those with rotation numbers that do not satisfy the Diophantine condition of the Kolmogorov – Arnold – Moser theorem. The cantori are invariant sets having a Cantor structure with gaps whose topological dimension is at least lower than the measure of the curve. The motion on them is quasi-periodic. However, cantori are unstable and therefore have stable and unstable manifolds. Unlike KAM tori, cantori are hardly permeable for passive scalars. The incoming flow contains particles at the intersection of a material line with the stable manifold Λ_s of the so-called chaotic invariant set Λ that reach the boundary between the mixing region and the vortex core in the course of time and rotate in a region as if their motion were limited by an invariant KAM curve. Then, they jump to the opposite side of the cantorus and stay there for a while. The process repeats many times until the particles cross the boundary of the region and escape. The existence of such sticky domains at the vortex-core and stable-island boundaries points to the existence of cantori with small gaps. They manifest themselves as domains with a large density of points on a Poincaré cross section. It is important that the existence of an invariant set of cantori and sticky domains implies that the mixing is inhomogeneous, as manifested, in particular, in topographic trapping maps by heavy power-law tails of trapping-time probability distribution functions and in singularities of scattering functions [23 – 26].

The chaotic invariant set Λ is a set of all trajectories (except for the KAM tori and cantori) that never leave the mixing region. The set consists of an infinite number of periodic trajectories and aperiodic chaotic ones. All trajectories in this set are unstable. Passive scalars with initial conditions belonging to Λ remain in the mixing region as $\tau \to \infty$ or $\tau \to -\infty$. The Poincaré cross section of Λ is a fractal set of points with Lebesgue measure zero. Most tracers from the incoming flow sooner or later leave the mixing region with the outgoing flow. But their behavior is largely determined by the presence of Λ. Tracers follow trajectories of this set, wandering for a long time in their neighborhoods.

Each orbit in the chaotic set and, therefore, the entire set Λ has both stable and unstable manifolds. The stable manifold Λ_s of the chaotic set is an invariant set of all the orbits approaching those in Λ as $\tau \to \infty$. The unstable manifold Λ_u is a stable manifold of time-reversed dynamics. Following trajectories in Λ_s, passive scalars from the incoming flow enter the mixing region and remain there forever. It was mentioned above that the corresponding initial conditions are in a set of measure zero. Tracers that are initially close to the trajectories of the stable manifold follow them for a long time and eventually deviate from them, leaving the mixing region along the unstable manifold. Thus, there is a unique opportunity to determine the important properties of Λ by measuring the characteristics of scattering particles and to observe unstable manifolds directly in laboratory experiments and even in geophysical flows.

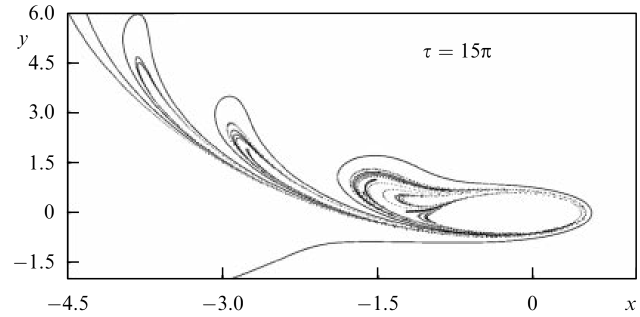

Figure 4. Image of unstable manifold (11) obtained as a 'snapshot' of a dye streak in the flow.

An unstable manifold can be visualized by various methods. An intricate fractal curve approaching Λ_u in the course of time is formed as a result of the deformation of a blob with many tracers chosen at the intersection of the incoming flow with the stable manifold. A similar picture is observed in experiments with dye streaks. Figure 4 shows an image of the unstable manifold of the deterministic model flow (12) at the time instant 15π, obtained numerically by integrating the equations of motion for particles continuously injected into the incoming flow at the point with coordinates $x_0 = -4.357759744$ and $y_0 = -6$. Passive particles are advected along the fractal curve of the unstable manifold, which is a kind of attractor in a Hamiltonian system (there are no 'classical' attractors in incompressible flows). Direct computation of the so-called trapping map [24] provides an image of the stable manifold Λ_s. The intersection of the manifolds Λ_s and Λ_u is the invariant chaotic set Λ, which is a fractal set of points oscillating with the period of the flow. Tracers starting from points of this set remain in the mixing region as $\tau \to \pm\infty$. In the unperturbed flow ($\xi = 0$), the border line between the vortex core and the free flow has a finite length equal to the length of the separatrix loop, but it is infinite in a flow with a periodic perturbation.

Periodic trajectories in the chaotic set Λ are essentially unstable, and the probability of finding them at the intersection of two fractal 'dust clouds' is low. A numerical method to prove their existence and to detect them was proposed in Ref. [27]. One computes the time $T_n(I, \theta)$ that a tracer with given initial values of the angle θ and action I takes to execute n turns and a change in the action [or in the energy $\Delta E_n(I, \theta)$] in this time. If the perturbation has a period T, then all the orbits of the perturbed system with the periods kT ($k = 0, 1, \ldots$), executing n turns, can be detected from the condition $T_n(I, \theta) = kT, \Delta E_n(I, \theta) = 0$. In fact, it is possible to detect periodic orbits arising due to a resonant structure of the phase space (elliptic and hyperbolic points of primary, secondary, and other resonances) and the orbits near separatrices. Examples of orbits detected for the model considered have been presented in Ref. [27].

3.2 Geometry of chaotic scattering and fractal dynamics

As an illustration of the geometry of the transport of passive scalars in the mixing region, we consider initial conditions on the segment of the line $y = -6$ in the free-stream region whose left endpoint is at the intersection of this line and the lower 'whisker' of the perturbed separatrix loop at the time $3\pi/2 + 2\pi m$ and whose right endpoint is at the intersection with the 'whisker' of the perturbed separatrix loop at $\pi/2 + 2\pi m$. Figure 5 shows fragments of the evolution of

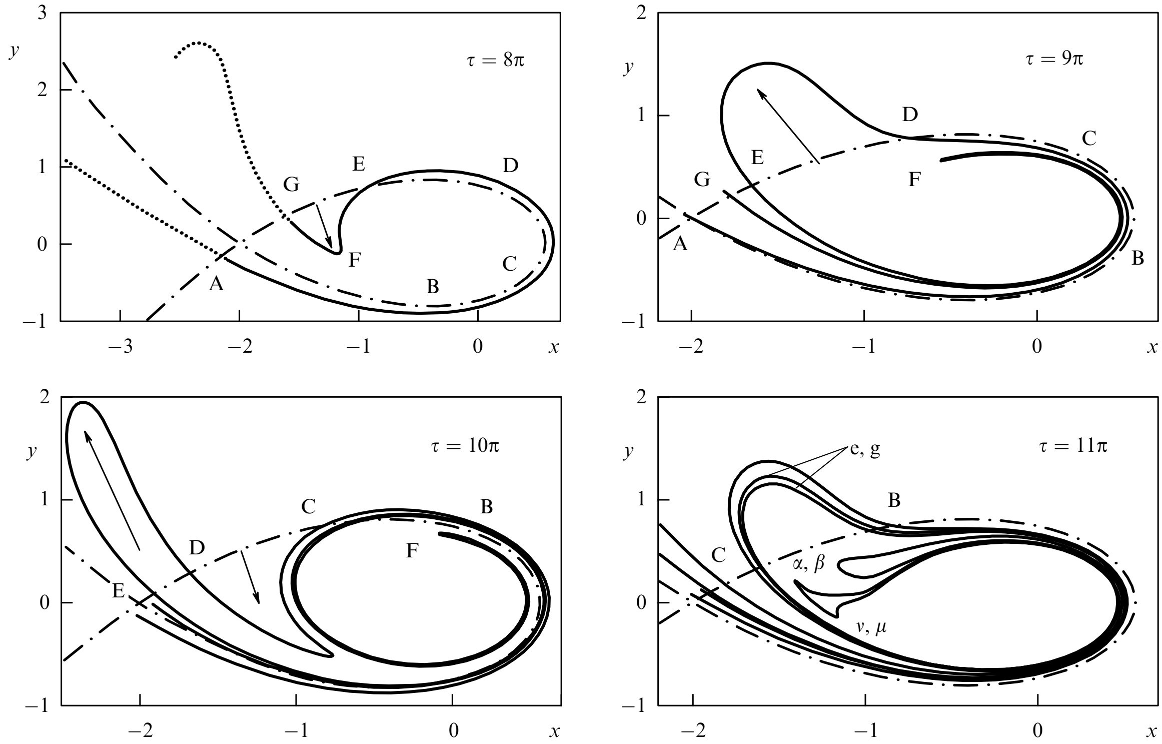

Figure 5. Evolution of a material line taken at successive instants to illustrate the development of lobes from elements of the epistrophes and strophes in the fractal shown in Fig. 6.

this material line at the instants $\tau = 8\pi$, 9π, 10π, and 11π. At $\tau = 0$, point A was at the intersection of the perturbed separatrix and the line $y_0 = -6$, and point G at the intersection of this line and the separatrix at the time $\pi/2 + 2\pi m$. The particles with initial positions $x_0 < x_0(\mathrm{A})$ and $x_0 > x_0(\mathrm{G})$ are not trapped in the vortex and are immediately washed away into the free-stream region (see dotted segments in Fig. 5). Particles A and G move along the stable manifold into the neighborhood of the saddle periodic orbit and remain in the mixing region for a long time (which is infinite in theory).

We compute the total number n of turns around the vortex executed by most particles placed initially at the segment AG before they escape into the outgoing free-stream region (the part of the plane above the line $y = 6$). The graph of $n(x_0)$ shown in Fig. 6 is a complicated hierarchy of sequences of fragments of the material line AG ('snapshots' of its evolution are shown in Fig. 5) with fractal properties that are generated by infinite intersections of the stable and unstable manifolds with the material line of initial conditions as it rotates around the vortex. There are sequences of segments for each $n \geqslant 0$, which we call 'epistrophes' following Ref. [28]. The epistrophes make up a hierarchy. The endpoints of each segment at the level n are the limit points of a level-$(n+1)$ epistrophe. For example, there is a single epistrophe at the level $n = 0$ converging at the point A. The endpoints of each segment of this epistrophe at the level $n = 1$ generate epistrophes b, c, d, e, g, etc., converging at the corresponding limit points (see Fig. 6). Numerical experiments on epistrophes lying at different levels reveal the following laws: (1) each epistrophe converges at a limit point in the segment under consideration; (2) the end points of each segment in a level-n epistrophe are the limit points of a level-$(n+1)$ epistrophe; (3) the lengths of segments in an epistrophe decrease in geometric progression;

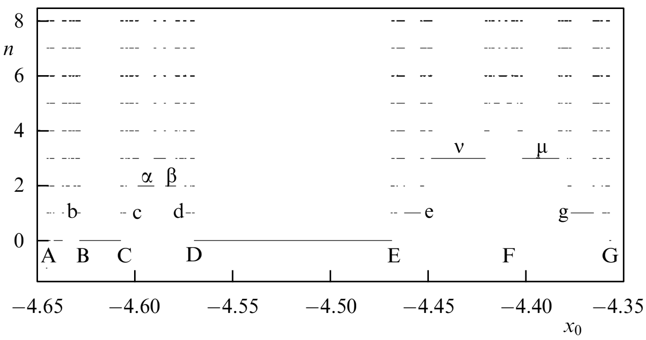

Figure 6. Fractal set (at $n \to \infty$) of the initial coordinates x_0 of incoming-flow tracers that escape from the mixing region after n turns around the vortex.

and (4) the common ratio of all progressions is equal to the maximal Lyapunov exponent for the chaotic invariant set λ. The length l_j of an epistrophe segment as a function of its index j for the zeroth-level epistrophe and the first-level epistrophes c, d, e, and g has been computed. The slopes of all graphs are equal to $\ln \lambda = -1.59$ [23], i.e., the segment lengths in each epistrophe decrease in geometric progression $l_j = l_0 \lambda^j$ with the ratio $\lambda \approx 0.2$. This quantity is the maximum Lyapunov exponent for the chaotic invariant set Λ.

The fractal in Fig. 6 is not strictly self-similar, because it contains segments, called strophes, that do not belong to the epistrophes. Some of them are labeled by Greek letters in the graph. Thus, the fractal is characterized by partial self-similarity: each level contains both self-similar epistrophe sequences and additional elements (strophes) that are preserved in the asymptotic limit and do not fit into the regular structure. The fractal in Fig. 6 provides a comprehensive illustration of tracer transport. Line segment AG stretches and bends as it winds around the point-like vortex, and then its part begins to fold as particles rotating around the vortex accelerate, while other particles decelerate in the neighborhood of the saddle point. Figure 5 illustrates the formation of the first fold at $\tau = 8\pi$. Segment DE is associated with the first segment of the zeroth-level epistrophe (tracers that have not made a complete turn). Segment EFG is represented by an empty segment in Fig. 6 generating an infinite sequence of strophes and epistrophes at the higher levels. After the period ($\tau = 10\pi$), the second fold develops in the material line. After the time interval $\tau = 11\pi$, two new lobes begin to develop in the stretched portion of the first fold corresponding to epistrophe segments e and g of the level $n = 1$. The particles in these lobes escape together with the lobe BC before they complete their second turn around the vortex, giving rise to the second 'finger' in Fig. 5. Furthermore, the snapshot taken at $\tau = 11\pi$ shows the folds that subsequently develop into the strophes α and β at the level $n = 2$ and into the strophes ν and μ at the level $n = 3$. These strophes give rise to four lobes that combine with zero- and first-level epistrophe segments to form the third 'finger.'

This process repeats iteratively, i.e., the part corresponding to an epistrophe segment and an empty segment in Fig. 6 unwinds off the material segment's 'tail' that fingers to the neighborhood of the saddle point with each turn around the vortex. This scenario describes the formation of epistrophes and strophes at all nonzero levels, except that each level-n epistrophe segment generates two level-$(n + 1)$ epistrophes. In experiments with dye tracks, these events are visualized by the periodic formation of lobe pairs. In the course of time, dye streamlines develop into a self-similar pattern (see Fig. 5) in the sense that new 'fingers' with an increasing number of lobes appear in each subsequent period. This reveals order hidden in chaos.

Rigorous definitions of invariant sets and dynamical invariant measures such as fractal dimensions, Lyapunov exponents, entropies, and transport and time exponents are given asymptotically, i.e., as $\tau \to \infty$. In reality, we are dealing with finite times and sizes. An exact self-similarity is absent (the existence of the strophes in our flow) in typical Hamiltonian systems with inhomogeneous mixing (the case of our model flow) because the invariant sets are not invariant in the statistical sense under increasing the resolution. Thus, the asymptotic behavior of dynamical systems may differ strongly from their behavior in a finite time, the only one that can be measured in computer and real experiments. It is meaningless from the physical standpoint to compute the fractal dimension of a hydrodynamic flow on spatial scales smaller than molecular ones and the Lyapunov exponent in a time exceeding the lifetime of a coherent Eulerian structure. The effective dimensions of dynamical 'invariants' to be computed may differ from asymptotic ones.

4. Kinematic models for chaotic advection in the ocean

Western boundary currents, like the Kuroshio in the North Pacific and the Gulf Stream in the North Atlantic, are prominent jets separating water masses with different physical and biogeochemical characteristics. Three basic mechanisms of transport and water-mass exchange in those frontal regions are known: the generation of so-called rings with a cold or warm core, which may separate from the main stream from both sides; interaction of the rings with the main stream; and meandering of the jet. Such currents are coherent Eulerian structures whose spatial form varies in time in a wavy manner in a wide range (with the wavelength of the order of 200 – 400 km) with typical values of the phase speed of the order of 0.1 – 0.3 m s^{-1} (for comparison, the maximum speed at the surface reaches 2 m s^{-1}). Observations of Lagrangian trajectories of neutrally buoyant floats, launched at different depths in both the Kuroshio [29, 30] and the Gulf Stream [31, 32], reveal large-scale lateral displacements of the floats in the absence of rings correlating with the meanders of the stream. Resuming those and other observations in the Gulf Stream, A Bower and H Rossby [32] came to the following conclusions: (1) water from the center of the stream is most often lost from the current at the trailing edges of a meander through troughs and crests, while entrainment occurs primarily at the leading edges of meander crests; (2) entrainment and transport of water masses across the stream are enhanced with an increase in the curvature of the jet; (3) cross-stream transport at lower depths occurs much more easily than near the surface. The Gulf Stream is more 'transparent ' for deep-water floats than for shallow-water ones.

In Fig. 7, we show a composition of 37 trajectories of RAFOS isopicnal floats (floats directly tracking the motion of fluid parcels in a flow) launched in the main thermocline near Cape Hatteras ($\sim 35°$N, $\sim 75°$W) and tracked acoustically for 30 or 45 days [32]. The evident irregularity of the trajectories raises the question of the mechanisms of transport and mixing of the physical, chemical, and biological properties of the Gulf Stream and similar oceanic fronts. The question of whether the trajectories of floats are chaotic is very important for the problem of the lateral mixing of passive scalars in the ocean [33 – 38]. The contribution of rings to the entire oxygen transport across the Gulf Stream was estimated to be less than 5% [39]. Chaotic advection has been regarded as the main mechanism of mixing in meandering jet currents [40].

First kinematical and then dynamical models have been proposed to explain observations quantitatively. The interpretation of Lagrangian motion is simplified by considering a flow in a reference frame moving with the phase speed of a periodic dominant meander. As the simplest kinematic model of a meandering jet current in the fixed frame, we take the

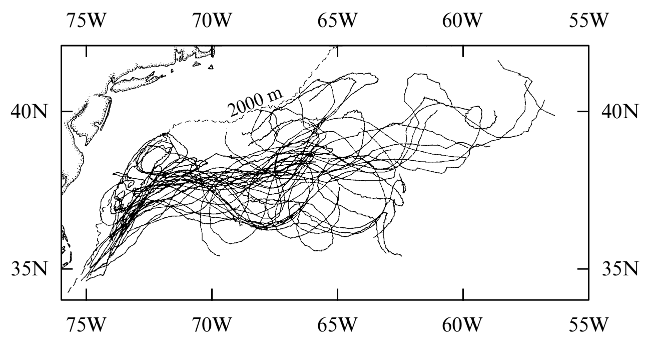

Figure 7. Composition of trajectories of RAFOS floats at the depth of the Gulf Stream thermocline [32]. Courtesy of A Bower (Woods Hole Oceanographic Institution, Woods Hole, USA).

streamfunction [39, 40]

$$\Psi(x,y,t) = \Psi_0\left(1 - \tanh\frac{y - a\cos k(x-c_x t)}{d\sqrt{1+k^2a^2\sin^2 k(x-c_x t)}}\right), \quad (14)$$

where $a, k = 2\pi/l$, and c_x are respectively the amplitude, wave number, and phase speed of the meander, l is the meander wavelength, and d a characteristic width of the jet. The hyperbolic tangent occurring in streamfunction (14) is related to the choice of the Bickley profile $u = u_0 \operatorname{sech}^2 y$ for the horizontal velocity in the jet, and the square-root term in (14) is inserted to ensure a uniform jet width through the meander. The normalized streamfunction in the frame moving with the phase speed c_x is

$$\Psi'(x', y', \tau) = -\tanh\left(\frac{y' - A\cos x'}{L\sqrt{1+A^2\sin^2 x'}}\right) + Cy', \quad (15)$$

where $x' = k(x - c_x t)$ and $y' = y/k$. The respective advection equations with streamfunction (15) and the normalized time $\tau = \Psi_0 k^2 t$ (primes omitted),

$$\begin{aligned} \dot{x} &= \frac{1}{L\sqrt{1+A^2\sin^2 x}\cosh^2\Theta} - C, \\ \dot{y} &= -\frac{A\sin x\,(1 + A^2 - Ay\cos x)}{L(1+A^2\sin^2 x)^{3/2}\cosh^2\Theta}, \\ \Theta &= \frac{y - A\cos x}{L\sqrt{1+A^2\sin^2 x}} \end{aligned} \quad (16)$$

involve three control parameters: the normalized meander amplitude $A = ak$, the jet width $L = dk$, and the phase speed $C = c_x/\Psi_0 k$. An analysis of Eqns (16) allows concluding [41] that in the comoving frame, there are a few topologically different regimes of motion determined by values of the phase speed C.

(1) For $C > C_{\mathrm{cr1}} = 1/L$, there are no stationary points.

(2) For $C_{\mathrm{cr1}} > C > C_{\mathrm{cr2}} = 1/\left(L\cosh^2(1/AL)\right)$ and $C > C_{\mathrm{cr3}}$, there are four stationary points: two centers and two saddles. There are two separatrices, each of which passes through its own saddle point. The free flow between the separatrices is directed westward.

(3) For $C_{\mathrm{cr1}} > C > C_{\mathrm{cr2}}$ and $C < C_{\mathrm{cr3}}$, the stationary points are the same as in the preceding case, but the free flow between the respective separatrices is directed eastward.

(4) For $C_{\mathrm{cr2}} > C > C_{\mathrm{cr3}}$, there are eight stationary points: four centers and four saddles. The free flow between the separatrices is directed westward.

(5) For $C_{\mathrm{cr2}} > C$ and $C < C_{\mathrm{cr3}}$, the stationary points are the same as in the preceding case, but the free flow between the respective separatrices is directed eastward.

Bifurcations arise if C is equal to one of the critical values C_{cr1}, C_{cr2} or C_{cr3}, with different relations between the critical values. It is difficult to find C_{cr3} analytically, but it can be shown that $C_{\mathrm{cr3}} > C_{\mathrm{cr2}}$ if

$$2(1+A^2)\left(AL\sinh\frac{2}{AL}\right)^{-1} < 1\,.$$

Otherwise, $C_{\mathrm{cr3}} < C_{\mathrm{cr2}}$.

Figure 8a shows trajectories of particles in the fixed frame in topological case (3) with values of the parameters estimated to be realistic fot the Gulf Stream. Because Ψ depends on time in the fixed frame, particles cannot intersect streamlines. In the comoving frame, we have $\Psi = \mathrm{const}$, and particle trajectories coincide with the streamlines shown in Fig. 8b. There are three different regions: the central eastward jet (region J), closed circulations to the north and south from the jet (regions C, sometimes called 'cat eyes' in the theory of dynamical systems), and the peripheral westward currents (regions P). The centers of the 'cat eyes' lie at two critical lines determined by the conditions $u(y_c) = c_x$ and $v(y_c) = 0$. The regions are separated from each other by separatrices connecting the equilibrium saddle points. Exchange between them is therefore impossible. These structures disappear, of course, in the fixed frame. Trajectories of advected particles are rather diverse. Particles launched in the jet core move eastward in the jet along curved trajectories. Particles launched in domains where the central jet overlaps with one of the circulation regions move downstream in the jet along less curved trajectories and much more slowly, with the meander phase speed.

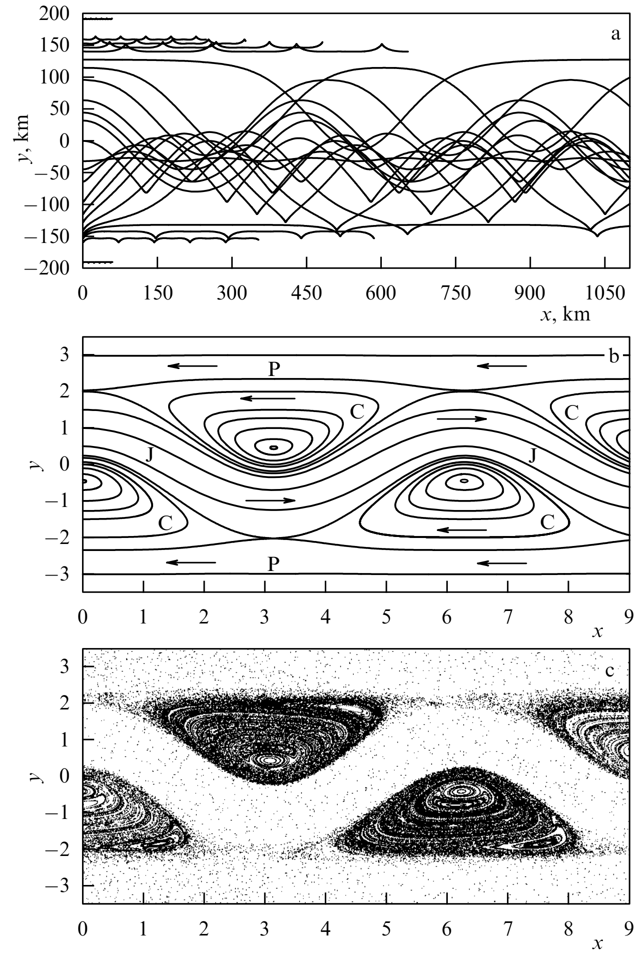

Figure 8. (a) Trajectories of particles in a meandering stream in the fixed frame; (b) streamlines in the reference frame moving with the meander phase speed; (c) Poincaré cross section with a periodically modulated meander amplitude.

It follows from the theory of dynamical systems that even a small nonstationary perturbation typically splits stable and unstable manifolds of saddle points. In the neighborhood of each of them, a stochastic layer arises in the manner described in Section 2.2. The resulting heteroclinic structure leads to chaotic mixing and the transport of water masses with flux values depending on many factors (the stochastic layer width,

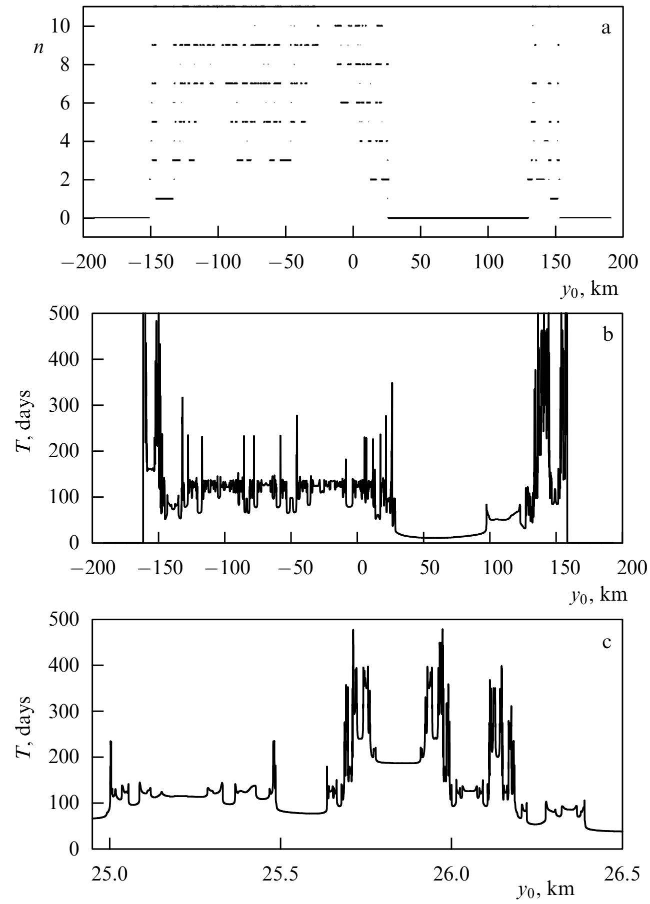

Figure 9. (a) Fractal dependence of the number of turns of particles n in the comoving frame on their initial latitude y_0; (b) time to reach a given longitude in the fixed frame depending on their initial latitude; (c) close-up of the small fragment in Fig. 9b.

the number of overlapping main resonances, etc.). Variations in the meander amplitude are assumed to be the main factor of the variability of the Gulf Stream and Kuroshio. Numerical simulation of the advection equations with a periodically modulated meander amplitude $A(\tau) = A_0 + \varepsilon\cos(\nu\tau + \varphi)$ confirms this assumption. With comparatively small perturbation amplitudes, $\varepsilon \ll 1$, the chaotic advection layer is narrow and the mixing is mainly zonal. Figure 8c shows a Poincaré cross section of the meandering current with a periodically modulated meander amplitude ($A = 0.785$, $C = 0.1168$, $L = 0.628$, $\nu = 0.117$, and $\varepsilon = 0.0728$). Because the perturbation amplitude is rather small (10% of the meander amplitude), only the outermost KAM tori are destroyed in the circulation regions where weak chaotic mixing is possible. Islands inside the circulation regions are related to resonances between the periodic perturbation and particle rotations in those regions.

As values of the perturbation ε increase, more and more invariant tori are destroyed, the area of the chaotic 'sea' increases, and there arise more islands of regular motion with sticking zones near their boundaries. As a result, the fractal dynamics of mixing and the transport of passive scalars occur. The fractal properties are illustrated in Fig. 9. Five thousand particles, distributed uniformly along the latitude $-200 < y_0 < 200$ km, are launched at zero longitude $x_0 = 0$ and the number of turns n (or the number of changes in the zonal velocity sign) is computed for each particle with the perturbation amplitude $\varepsilon = 0.2355$ and the frequency $\nu = 0.2536$. Figure 9a shows the dependence $n(y_0)$ in the comoving frame; the dependence has a Cantor-like structure (to be compared with Fig. 6). The dependence of the number of events $u = c_x$ on y_0 is similar in the fixed frame, where the sign of the zonal velocity does not change. In the fixed frame, the chaotic dependence of the instant T at which the floats reach a given longitude ($x_f = 1100$ km is taken in simulation) on their initial latitude is a direct consequence of the fractality of float trajectories in a real current. It is an irregularly oscillating function (Fig. 9b) consisting of chaotically alternating smooth and singular-like intervals. A close-up of singular-like intervals reveals a self-similar structure (Fig. 9c). A small initial difference in the float positions (of the order of 100 m) may cause a large difference in the drift time (around half a year). As the perturbation ε increases further, a meridional transport becomes possible.

In Fig. 10, to illustrate chaotic mixing of passive scalars, we show snapshots of the evolution of a material line (with 25,000 particles distributed initially at zero longitude $x_0 = 0$ along the latitude $-200 < y_0 < 200$ km) at successive instants. The periodic development of lobes from elements of the fractal depicted in Fig. 9a has been studied in detail by one of the present authors and colleagues [41].

Besides a periodic variation in the meander amplitude A, other types of periodic perturbations have been considered in the literature [40]: a spatially uniform meridional flow with the streamfunction $\Psi'_{\rm m} = x\cos(\nu\tau + \varphi)$ and a plane wave with the streamfunction $\Psi'_{\rm p} = p^{-1}\cos\left[p(x - c_{\rm p}\tau) + \varphi\right]$. Adding these functions to stationary function (15), we obtain new dynamical systems describing different types of a periodic perturbation of the basic flow (15). A periodicity of the perturbation simplifies solving the advection equations by reducing them to a Poincaré map, i.e., allowing consideration of a trajectory of a fluid particle in discrete time with an interval equal to the perturbation period. To model a quasi-periodic variability of a meandering jet, it is necessary to incorporate a few harmonics with incommensurate frequencies in a streamfunction.

The theory of dynamical systems provides a convenient measure for the transport and mixing of chaotically advected water masses based on the Melnikov integral (10). Estimates of meridional and zonal fluxes help us to determine distributions of potential vorticity, temperature, nutrients, and other characteristics of water masses in meandering currents. It is evident that the values of the fluxes depend on the topology of the phase portraits of the unperturbed system. The streamline picture in the comoving frame shown in Fig. 8b allows identifying two main fluxes: $F_{\rm jc}$ is a flux from the jet core J to the circulation regions C and $F_{\rm cp}$ is a flux from the circulation regions to the region of peripheral westward currents P. It follows from symmetry considerations that the corresponding fluxes for the northern and southern circulations (with respect to the jet) and the peripheral currents are equal. Calculations of the fluxes in Ref. [40] by means of Melnikov integral (10) show that the values $F_{\rm jc}$ and $F_{\rm cp}$ in the case of meandering with a fluctuating amplitude depend strongly on the perturbation frequency ν. For comparatively high frequencies ($\gtrsim 0.04$ cycles per day), we have $F_{\rm jc} > F_{\rm cp}$, whereas for low frequencies ($\lesssim 0.04$ cycles per day), we have $F_{\rm jc} < F_{\rm cp}$. Waves propagating along the meandering jet can enhance the fluxes if their phase speeds correspond to the speeds of the basic flow along the corresponding boundaries. Numerical simulation in Refs [40, 42] confirms the observa-

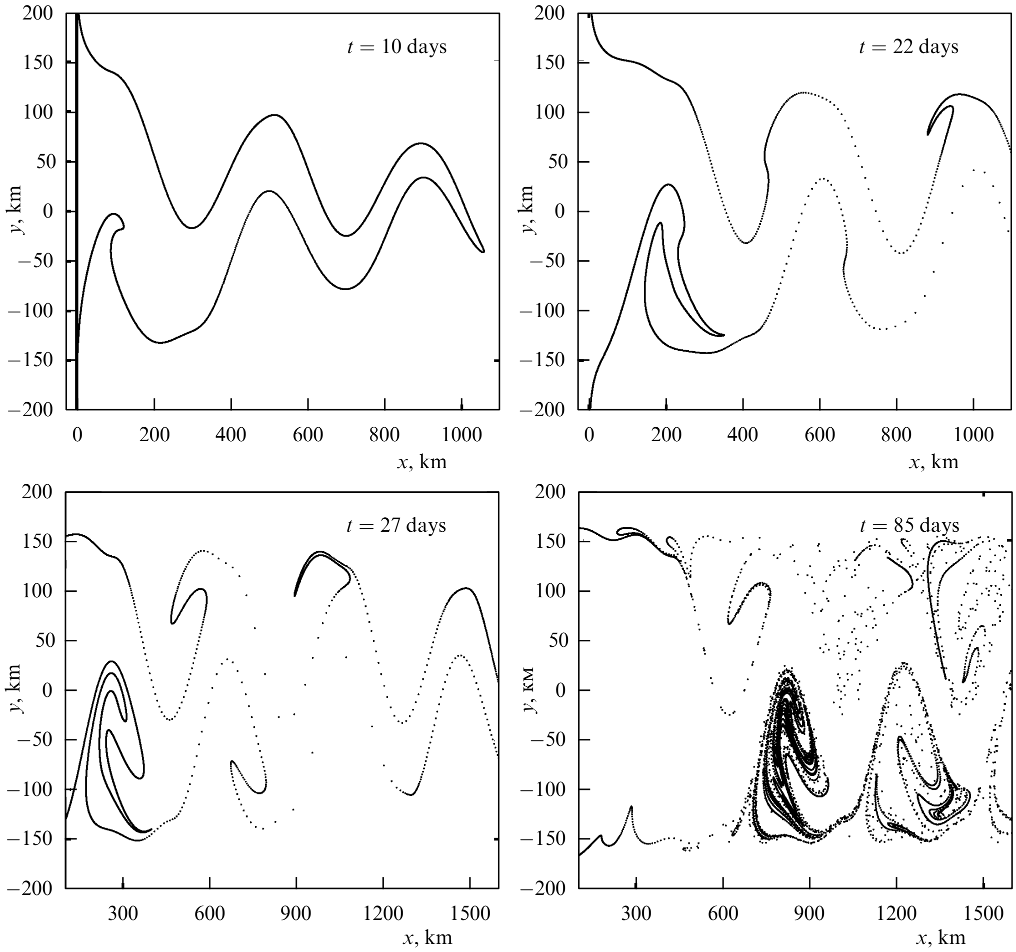

Figure 10. The evolution of a material line in a meandering current with a periodic modulation in the fixed frame. The development of lobes from elements of the fractal is shown in Fig. 9a.

tions: transport across the jet core is much smaller than the fluxes F_{jc} and F_{cp}. The meandering jet mixes fluid well along each of its sides but preserves gradients across the jet core. We emphasize that the conclusions are valid with a topological regime specified for the simple streamfunction (14) with periodic perturbations. Values of the fluxes calculated with the same system but under quasi-periodic perturbations may differ [43]. Mixing in the kinematic model of a meandering jet interacting with an eddy was calculated in Ref. [44].

An increase in meridional (cross-jet) transport with depth is quite evident in the RAFOS float observations mentioned above [31, 32]. The effect can be explained qualitatively in the framework of a multi-layer kinematic model in which the velocity $u(y, z)$ decreases monotonically with depth. The flow remains two-dimensional in the sense that passive scalars move over isopicnal surfaces, but the topology of the flow may differ for different isopicnal surfaces. The meander phase speed is constant but the velocity in the jet core decreases with depth (pressure). The critical lines $u(y_{\mathrm{c}}, z)$ converge as z increases (Fig. 8b) and coincide at some value $z = z_{\mathrm{c}}$. Instead of two chains of 'cat eyes' separated by a jet, a vortex street appears and the meridional transport becomes easier [32]. Furthermore, the meander amplitude also varies significantly with increasing the depth of such a transport. In recent paper [45], a dynamically consistent baroclinic (more exactly, with two and a half layers) model of a meandering current was proposed. In this model, meridional transport in a zonal flow is enhanced with depth as a result of a baroclinic instability arising when the ratio of velocities in the upper and lower layers is greater than 2.

Chaotic transport and mixing have been studied in a model with planetary gyres [46–48]. Two gyres, subpolar and subtropical, separated by a western boundary jet current (the Gulf Stream in the North Atlantic and the Kuroshio in the North Pacific) were considered. Circulation in the gyres is forced by surface wind. Intergyre water-mass exchange in the simple model of a two-dimensional incompressible flow is impossible if the wind is assumed to be steady. Interannual migration of the wind results in splitting and intersections of stable and unstable invariant manifolds; as a consequence, chaotic intergyre transport of water masses becomes possible. In the framework of the simplest kinematic model with a periodic perturbation, the maximum transport occurs for the frequencies resonant with the circulation frequency. Incorporation of meandering-jet streamfunction (14) in the two-gyre model results in an additional mixing mechanism. As stressed above, the meandering jet is itself a good barrier for meridional transport (at least in the undersurface layer). Wind forcing significantly enhances the intergyre chaotic meridional transport [47].

For three-dimensional flows, chaotic advection of passive scalars is possible even in the stationary case. It was mentioned above that this was first noted by V I Arnold [12]. A kinematic model with a three-dimensional circulation, consisting of two planetary horizontal gyres and a thermohaline vertical circulation, was proposed in Ref. [49]. The corresponding equations of motion for Lagrangian particles are not Hamiltonian but constitute a three-dimensional autonomous set of ordinary differential equations with chaotic solutions. It is important from the oceanographic standpoint that chaos in that model leads to a barrier to transport, which is related to the outermost unbroken KAM torus in the three-dimensional space.

Kinematic models are attractive due to their simplicity, generality, and the possibility of revealing the underlying geometric structures responsible for Lagrangian transport and mixing. Kinematic models allow obtaining analytic results and quantitative relations between topological, dynamical, and statistical characteristics of flows. But kinematical streamfunctions are not solutions of the dynamical equations of motion and the potential vorticity is not conserved in kinematic models in general. The concept of background currents allows obtaining, in a closed form, a class of dynamically consistent streamfunctions with specified basin forms, bottom topography, and debits at boundaries. In Section 5, this concept is used to construct a few classes of streamfunctions in barotropic and geostrophic approximations in order to study chaotic advection in dynamically consistent models for basins of Far Eastern margin seas, which are known to have a high intraannual variability of mass fluxes through their straits.

5. Dynamical models of chaotic advection in the ocean

The kinematics of an incompressible plane fluid flow is described by a streamfunction $\psi(x, y, t)$ related to the velocity components (4) and vorticity ω as

$$\omega = v_x - u_y \equiv \Delta\psi \, . \tag{17}$$

If the streamfunction ψ is specified disregarding the laws of fluid motion, then (5) is a kinematic model. The problem of dynamical compatibility lies in the fact that ψ must satisfy relations following from dynamical equations. The first nontrivial geophysical two-dimensional and dynamically consistent model with deterministic chaos seems to have been analyzed using a classical Kida vortex [50, 51]. As promising models for studying chaotic advection, we consider a class of simple dynamically consistent models proposed by V F Kozlov [4, 52, 53], based on the concept of background currents in geophysical hydrodynamics.

5.1 Background currents

In dynamical oceanography, the notion of a background current, by which one understands an averaged (in a sense) circulation, is commonly used. As a rule, definitions of that notion (if they are given at all) are not productive either because they do not allow uniquely constructing the corresponding background current or because it is impossible to actually realize the 'averaging' due to the lack of information about the fields to be averaged (e.g., in view of the lack of observational data), in deep water in particular. An attempt to give one possible constructive definition of a background current was made in Ref. [53]. We illustrate the main idea of the method proposed with a simple example [52].

One of the basic characteristics of quasi-two-dimensional geophysical flows is the potential vorticity Π, which combines contributions of the relative vorticity ω and planetary-topographic interactions, which are generally complicated by stratification. Because Π and ω are linearly related, fixing either of them allows determining the velocity field unambiguously for the corresponding boundary conditions. Both Π and ω can be used to distinguish between coherent structures such as vortices, jets, and fronts. Traditionally, it is preferable to use the relative vorticity ω. In contrast, the potential vorticity Π is a Lagrangian invariant in the absence of viscosity and satisfies the equation

$$\frac{\mathrm{d}\Pi}{\mathrm{d}t} \equiv \Pi_t + u\Pi_x + v\Pi_y = 0 \, . \tag{18}$$

Owing to its invariance, the potential vorticity Π is a more convenient quantity for determining the current structure. As the background current (a reference current, in other words), it is reasonable to take a current with the horizontally homogeneous and stationary distribution of Π satisfying Eqn (18) by definition. But the result depends on the value of Π because the current structure can change drastically as its value varies. From this set of solutions, we single out the one for which $\Pi = \bar{\Pi}$ provides a global minimum for the system mechanical energy. Simultaneously, we determine the background relative vorticity $\bar{\omega}$ depending on the bottom relief, planetary vorticity, and stratification in the baroclinic case. The evolution of any given initial state can then be studied as the interaction of corresponding deviations of Π from the background value $\bar{\Pi}$, which is independent of those perturbations.

We consider the algorithm for constructing a background current and the corresponding distributions of background relative vorticities using the simplest quasi-geostropic barotropic model [51], for which we have [53]

$$\Pi = \omega + F \, , \tag{19}$$

where $F = f(x, y) + (f_0/H)\, h(x, y)$ is a given planetary-topographic function, including contributions from the Coriolis parameter $f(x, y)$ with a reference value f_0, the mean basin depth H, and the topographic bottom evaluation $h(x, y)$. We consider a current in a basin D with the boundary ∂D described by Eqns (18) and (19), and with the function $\psi^{(\mathrm{b})}(l, t)$ determining debits at the boundary (l is the coordinate of a point on the boundary):

$$\psi \Big|_{\partial D} = \psi^{(\mathrm{b})}(l, t) \, . \tag{20}$$

Using (19) and (20), we can find the relations for the derivative with respect to the parameter $\Phi \equiv \partial\psi/\partial\Pi$:

$$\Delta\Phi = 1 \, , \qquad \Phi \Big|_{\partial D} = 0 \, . \tag{21}$$

Taking (19) and (21) into account, we obtain the kinetic energy

$$E = \frac{1}{2} \int_D (\nabla\psi)^2 \, \mathrm{d}D \tag{22}$$

and, after simple transformations, the necessary minimum condition

$$\frac{\partial E}{\partial \Pi} = \int_D \Phi(F - \Pi) \, \mathrm{d}D = 0 \, , \tag{23}$$

which implies

$$\bar{\Pi} = \langle F \rangle \equiv \left(\int_D F\Phi \, \mathrm{d}D \right) \left(\int_D \Phi \, \mathrm{d}D \right)^{-1} . \qquad (24)$$

The right-hand side of this relation determines a weighted averaging of an arbitrary function F with the condition $F_{\min} \leqslant \langle F \rangle \leqslant F_{\max}$, which is always satisfied. Thus, a background current is determined unambiguously by a given distribution of the background relative vorticity $\bar{\omega}$ as a solution of the Dirichlet problem

$$\Delta\bar{\psi} = \bar{\omega} \equiv \langle F \rangle - F , \qquad \bar{\psi}\Big|_{\partial D} = \psi^{(\mathrm{b})}(l, t) . \qquad (25)$$

With the expression for F, we obtain

$$\bar{\omega} = \bar{\omega}^{(h)} + \bar{\omega}^{(f)} , \qquad \bar{\omega}^{(h)} = \frac{f_0}{H}\big(\langle h \rangle - h\big) , \qquad \bar{\omega}^{(f)} = \langle f \rangle - f . \qquad (26)$$

The constants $\langle h \rangle$ and $\langle f \rangle$ determine a critical isobath and a latitude at whose intersection the corresponding components of $\bar{\omega}$ reverse signs. In the northern hemisphere, $f > 0$ and the vorticity $\bar{\omega}^{(f)}$ is cyclonic (anticyclonic) to the north (to the south) from the critical latitude. Analogously, $\bar{\omega}^{(h)}$ is cyclonic (anticyclonic) in regions where depths are larger (smaller) than the critical one. In particular, the background topographic circulation above bottom elevations is anticyclonic. A formal solution of problem (25) is easily written in an explicit form (in quadratures) if the Green's function $G(\mathbf{r}, \boldsymbol{\rho})$ for the Laplace operator with the boundary condition $G\big|_{\partial D} = 0$ is known. We have [55]

$$\bar{\psi}(\mathbf{r}, t) = \bar{\psi}^{(\omega)}(\mathbf{r}) + \bar{\psi}^{(\mathrm{b})}(\mathbf{r}, t) , \qquad (27)$$

where the first term in the right-hand side,

$$\bar{\psi}^{(\omega)}(\mathbf{r}) = \int_D G(\mathbf{r}, \boldsymbol{\rho}) \, \bar{\omega}(\rho) \, \mathrm{d}D_\rho , \qquad (28)$$

is the steady vortical part of the solution, and the second term,

$$\bar{\psi}^{(\mathrm{b})}(\mathbf{r}, t) = \int_{\partial D_\rho} \bar{\psi}^{(\mathrm{b})}(l_\rho, t) \, \frac{\partial G}{\partial h_\rho} \, \mathrm{d}l_\rho , \qquad (29)$$

is the unsteady nonvortical part conditioned by the debits at the boundary.

In the absence of dissipation and generation, the potential vorticity homogenization Π is justified theoretically in a simple way for regions with closed streamlines [56]. The fluxes on the boundary of the domain D, allowed in our approach, have no ventilation effect because, by definition, they import and export the potential vorticity Π whose value is adjusted to that inside the region [53]. On the other hand, it follows from Eqn (26) that the planetary-topographic vorticity has a zero weighted average value, i.e., it resembles a dipole structure revealed in individual circulation rings. The potential vorticity is homogenized in the course of time, but the corresponding values of Π are different in individual circulation rings, which naturally leads to the problem of fronts in the field Π appearing in a background current. As a result, we face the problem of the combined evolution of the fronts Π and vortices in a current [57]. In Refs [58–60], an attempt was made to apply the developed algorithms to the construction of background currents in specific physical and geographical conditions in the Russia Far-Eastern margin seas. Examples of model background currents on the half-plane with a balanced source–sink system placed at its boundary have been considered in Ref. [61].

In the quasi-geostrophic approximation of a two-layer ocean with constant densities in the layers ρ_i ($i = 1, 2$ in the upper and lower layers, respectively), the motion is described by geostrophic streamfunctions $\psi_i(x, y, t)$. Equations (4), (5), (17), and (18) describe the corresponding values in the layers. The potential vorticity can be written as

$$\Pi_i = \omega_i + F_i - \Pi_i^* , \qquad (30)$$

where $F_1 = f + (f_0/H_1)\zeta$, $F_2 = f + (f_0/H_2)(h - \zeta)$, ζ and h are elevations of the interface and of the bottom relief, respectively, H_i is the thicknesses of the layers ($H = H_1 + H_2$), and Π_i^* is to be defined below. In accordance with the dynamical condition of the pressure continuity at the interface, we obtain

$$\zeta = \frac{f_0}{g'} \, (\psi_2 - \psi_1) ,$$

where $g' = g(\rho_2 - \rho_1)/\rho_2$ is the reduced acceleration of gravity. Following Ref. [53], we introduce baroclinic and barotropic streamfunctions $\psi = (H_1\psi_1 + H_2\psi_2)/H$ and $\psi' = (f_0/g')\zeta = \psi_2 - \psi_1$ and the corresponding potential vorticities $\Pi = (H_1\Pi_1 + H_2\Pi_2)/H$ and $\Pi' = \Pi_2 - \Pi_1$. Using Eqn (17), we obtain

$$\Delta\psi = \Pi - F + \Pi^* , \qquad (31)$$

$$\Delta\psi' - k^2 = \Pi' - \frac{f_0}{H_2} \, h + \Pi^{*\prime} , \qquad (32)$$

where $k^{-1} = L_{\mathrm{d}} = (g' H_1 H_2 / H_2)^{1/2} / f_0$ is the internal deformation radius. We introduce the weighted averaging

$$\langle F \rangle_k = \left(\int_D F\Phi^{(k)} \, \mathrm{d}D \right) \left(\int_D \Phi^{(k)} \, \mathrm{d}D \right)^{-1} \qquad (33)$$

with a weight function that satisfies the equation

$$\Delta\Phi^{(k)} - k^2\Phi^{(k)} = 1 , \qquad \Phi^{(k)}\Big|_{\partial D} = 0 , \qquad (34)$$

and define the parameters

$$\langle \Pi^* \rangle = \left\langle f + \frac{f_0}{H} \, h \right\rangle , \qquad \langle \Pi^{*\prime} \rangle = \frac{f_0}{H_2} \langle h \rangle .$$

The solutions of Eqns (31) and (32) for constant mean values of the potential vorticities are given by

$$\psi = \bar{\Pi}\Phi + \bar{\psi} , \qquad \psi' = \bar{\Pi}'\Phi^{(k)} + \bar{\psi}' , \qquad (35)$$

where

$$\Delta\bar{\psi} = \langle f \rangle_0 - f + \frac{f_0}{H}\big(\langle h \rangle_0 - h\big) , \qquad \bar{\psi}\Big|_{\partial D} = \psi^{(\mathrm{b})}(l, t) , \qquad (36)$$

$$\Delta\bar{\psi}' - k^2\bar{\psi}' = \frac{f_0}{H_2}\big(\langle h \rangle_k - h\big) , \qquad \bar{\psi}'\Big|_{\partial D} = \psi^{(\mathrm{b})\prime}(l, t) . \qquad (37)$$

As in the barotropic case, the energy minimum is achieved at $\bar{\Pi} = \bar{\Pi}' = 0$ [53], i.e., for the background currents $\psi = \bar{\psi}$ and $\psi' = \bar{\psi}'$. The geostrophic streamfunctions in the layers are given by [54]

$$\bar{\psi}_1 = \bar{\psi} - \frac{H_2}{H}\,\bar{\psi}\,', \qquad \bar{\psi}_2 = \bar{\psi} + \frac{H_1}{H}\,\bar{\psi}\,', \tag{38}$$

which shows the weakening role of stratification in topographic effects in the upper layer. The planetary background current is of a purely barotropic nature.

5.2 A semicircular basin

According to the concept of background currents [53], the streamfunction has the structure in Eqn (27), where the stationary planetary component ψ_1 is vortical ($\Delta\psi_1 = \omega$ in the region D and $\psi_1|_{\partial D} = 0$) and the incident-flow nonstationary component ψ_2 is nonvortical ($\Delta\psi_2 = 0$ and ψ_2 is fixed at the boundary ∂D).

As the first example, we consider a semicircular basin $x^2 + y^2 < a^2$, $y > 0$ with a source and a sink of intensities $\pm q(t)$ at the corner points $(-a, 0)$ and $(a, 0)$, respectively [61]. Assuming that in the β-plane approximation $f = f_0 + \beta^* y$, the bottom relief elevation is $h = -\gamma h_0 y/a$ (the depth linearly increases northward if $\gamma > 0$), it is easy to obtain

$$\psi_1 = -\frac{\beta}{8}(a^2 - x^2 - y^2)\,y\,, \tag{39}$$

where the constant parameter

$$\beta = \gamma\,\frac{f_0 h_0}{Ha} - \beta^* \tag{40}$$

is expressed in terms of the mean value of the Coriolis parameter f_0, the Rossby parameter β^*, the mean basin depth H, the elevation scale of bottom relief h_0, and the meridional slope of bottom relief γ. In what follows, we assume that $\beta > 0$, i.e., the topographic effect is stronger than the planetary one, as, for example, in the Sea of Japan [58]. The incident-flow component has the form

$$\psi_2 = -\frac{2q}{\pi}\arctan\frac{2ya}{a^2 - x^2 - y^2}\,. \tag{41}$$

Passing to dimensionless variables in accordance with the relations

$$(x, y) = a(x', y')\,, \qquad t = \frac{8}{\beta a}\,t'\,,$$
$$\psi = \frac{\beta a^3}{8}\,\Psi'\,, \qquad q = \frac{\pi\beta a^3}{8}\,\sigma(t') \tag{42}$$

and omitting the primes, we finally obtain

$$\Psi = -(1 - x^2 - y^2)\,y - 2\sigma(t)\arctan\frac{2y}{1 - x^2 - y^2}\,, \tag{43}$$

where $\sigma(t)$ is a given positive-valued function of time corresponding to the dimensionless debit $\pi\sigma$.

An instantaneous pattern of streamlines, which is symmetric with respect to the axis $x = 0$, is determined by a corresponding value of $\sigma(t)$. An elementary analysis of the velocity field shows that if $\sigma > 1$ (subcritical regime), the incident-flow component is dominant and the flow is quantitatively identical to a purely incident current produced by the source–sink system at corner points. If $\sigma = 1$, the velocity vanishes at the point $(0, 1)$. At $\sigma < 1$ (supercritical regime), this point splits into three critical points, two hyperbolic ones lying on the semicircle $r = 1$ at azimuthal angles $\theta = \theta_1$ and $\theta = \pi - \theta_1$ and an elliptic one $(0, y_0)$ lying

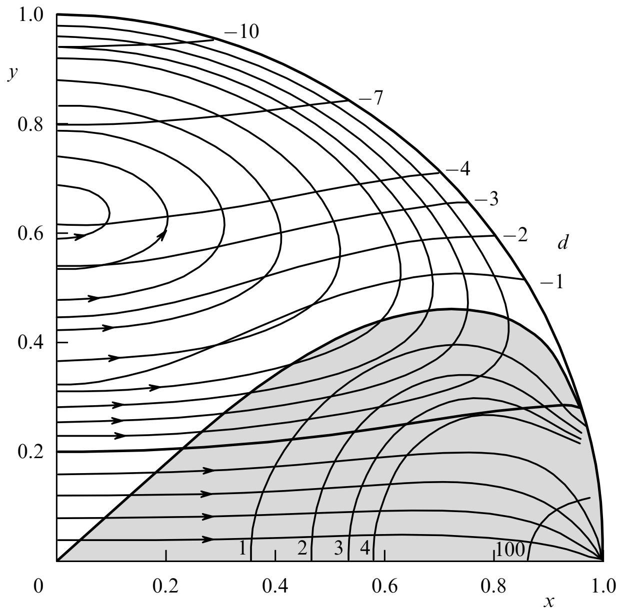

Figure 11. Plot of field isolines d with specified values and streamlines (shown by arrows) with the separatrix in the stationary case ($\sigma = \sigma_0$). The instability region $d > 0$ is shadowed.

on the semidiameter $x = 0$. The corresponding streamlines are plotted in Fig. 11. A separatrix (heteroclinic trajectory) with $y_1 = \min y$ and $y_2 = \max y = \sin\theta_1$ divides the incident-flow region adjacent to the diameter $y = 0$ from the overlying vortex region with the center at $(0, y_0)$. Using Eqn (43), we find the explicit relations

$$y_0^2 = \frac{1}{3}\left(2\sqrt{1 + 3\sigma} - 1\right), \qquad y_2 = \sqrt{\sigma} \tag{44}$$

and the transcendental equation

$$\sigma = \frac{(1 - y_1^2)\,y_1}{4\arctan\left[(1 - y_1)/(1 + y_1)\right]}\,. \tag{45}$$

In the stationary case with $\sigma < 1$, it is easy to estimate some characteristic times. The time it takes for a particle to pass through the diameter $y = 0$ is

$$t_{\mathrm{d}} = \int_{-1}^{1}\frac{\mathrm{d}x}{u(x, 0)} = F\big(\sqrt{1 + 4\sigma}\,\big)\,, \tag{46}$$

where a monotonically decreasing function of the parameter p is introduced:

$$F(p) = \frac{1}{2p}\left[\sqrt{\frac{p+1}{2}}\,\ln\frac{\sqrt{(p+1)/2} + 1}{\sqrt{(p+1)/2} - 1} - 2\sqrt{\frac{p-1}{2}}\,\arctan\frac{1}{\sqrt{(p-1)/2}}\right]. \tag{47}$$

In the neighborhood of the point $(0, y_0)$, we can find the time of particle revolution by approximating trajectories by ellipses:

$$t_0 = \frac{\pi(1 + y_0^2)}{2y_0\sqrt{(1 - y_0^2)(1 + 3y_0^2)}}\,. \tag{48}$$

The function $t_0(\sigma)$ has a weakly pronounced minimum in the neighborhood of $\sigma = 0.17$.

If $\sigma(t)$ is a positive-valued periodic function, then the separatrix and hyperbolic end points oscillate periodically. From the topological standpoint, this model resembles the model in Refs [46, 62], and one may expect the occurrence of chaotic advection. However, this model is open due to a free current, unlike, for example, the models considered in Refs [63–65].

The occurrence of chaos in nonautonomic systems of the type $\dot{x} = u(x, y, t)$, $\dot{y} = v(x, y, t)$ is closely related to the stability properties of individual fluid particles. But these problems are not equivalent [66]. A local analysis of the linear stability of solutions reduces to studying eigenvalues of a linearized matrix which, in the case of incompressible fluid $(u_x + v_y = 0)$, satisfies the equation [2]

$$\lambda^2 = d \equiv v_x u_y - v_y u_x \,. \qquad (49)$$

Because d is an even function of x and y, it is necessary to analyze its behavior in the first quarter of the circle $x^2 + y^2 \leqslant 1$ (see Ref. [61] for details). It turns out that in general, the curve of neutral stability $d = 0$ intersects the separatrix at the boundary approaching the intersection point from 'above.' On the other hand, the separatrix always intersects the circular boundary horizontally, and hence there is one more (besides the boundary one) 'internal' point where the separatrix intersects the curve $d = 0$. The neutral stability curve lies to the right of this point up to the boundary, and therefore the streamlines adjacent to the separatrix lie at least in the linear instability region in some intervals. In these intervals, fluid particle trajectories manifest unstable behavior and mix in a chaotic manner. In Fig. 11, we show streamlines with a separatrix and field isolines d computed for the stationary case $\sigma = \sigma_0$ [67].

In numerical experiments, the debit was specified as

$$\sigma = \sigma_0 \left[1 + \varepsilon \sin(\nu t + \varphi) \right], \qquad 0 < \varepsilon < 1 \,, \qquad (50)$$

where the parameter $\sigma_0 = 0.081632$ was chosen from the condition that in the stationary case $(\varepsilon = 0)$, the width of the incident-flow region in the central section $x = 0$ be the fifth part of the radius. The other parameters were varied. The law of the variation of $\sigma(t)$ in (50) determines a perturbation of Hamiltonian (43), and, in principle, allows applying variants of the asymptotic perturbation theory, for example, the Melnikov integral method (see Section 2.2). Numerical experiments have shown that depending on the initial positions and parameter values, three types of trajectories are possible: those remaining in the incident-flow region (with subsequent washing out through the sink) or in a vortex region or those penetrating from one region into another with possible returns. In particular, the problem of washing out the tracers from a vortex region into an incident-flow one is of interest.

Application of the standard methods for estimating the strength of chaos, such as Poincaré cross sections and Lyapunov exponents, is difficult in the present case because the lifetime of particles with chaotic behavior is limited in open systems. A repeated injection of particles [68] washed out through the sink is not justified because of singularities that do not allow restoring a trajectory of the injected tracer outgoing from the source, as is possible in open systems satisfying the boundary conditions of periodicity and continuity of the velocity field [69]. Therefore, the only possibility, perhaps, is an analysis of the distribution of Lyapunov exponents computed for a finite time by the method proposed in Ref. [66]. It has been stressed in [70] that from the physical standpoint, we are always interested in finite-time effects. One more interesting characteristic is the lifetime of tracers in the vortex region [67]. An analysis of washing out of a collection with 8300 tracers, initially uniformly distributed over the basin, has been carried out previously. The time of tracer washout through the sink was computed. The results are shown in Fig. 12 with the initial phases φ and the optimum (for the washing out) values of other parameters indicated. In all the cases, we can distinguish the regions with 'long-lived'

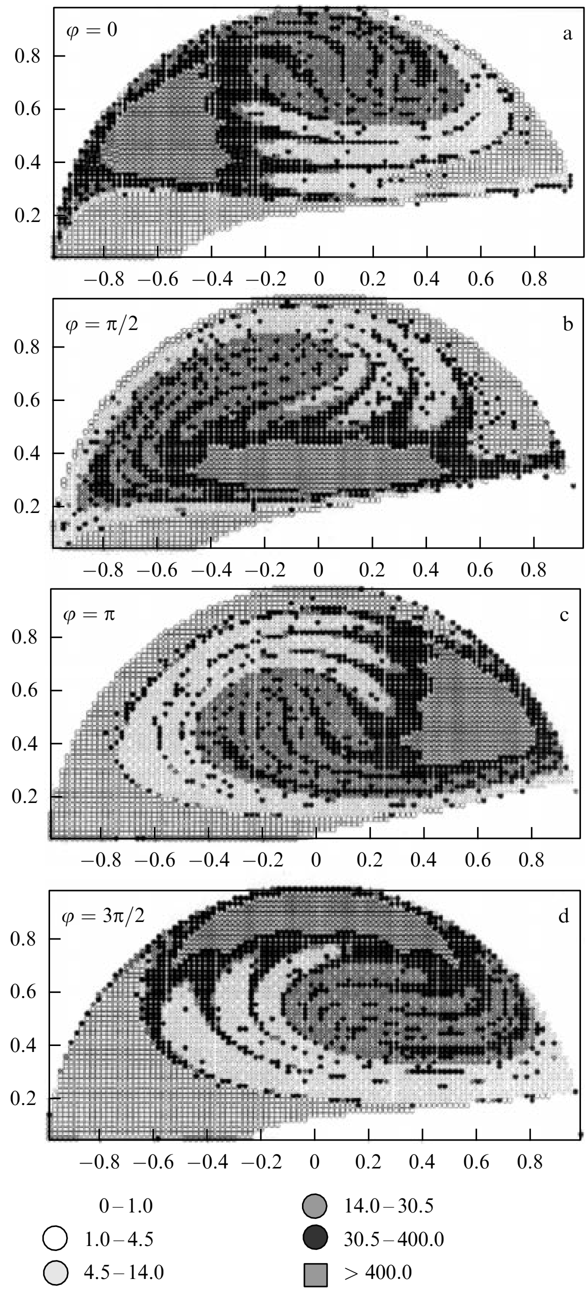

Figure 12. Distribution of times of tracer washout through the sink on their initial positions with specified values of the initial perturbation phase. The parameters are $\nu = 1.875$ and $\varepsilon = 0.5$. Tracers with normalized washout times less than 1 are situated in the white region in the lower right corners in figs a–d.

tracers, which shift along the boundary of the vortex region counterclockwise with increasing the phase. Comparison of the distributions of finite-time Lyapunov exponents corresponding to the initial positions of the tracers with the same values of parameters as in Fig. 12 with $\varphi = 0$ [67] allows regarding a finite-time Lyapunov exponent as a reliable indicator of the chaotic character of corresponding trajectories. In [67], dependences of washout times for 10,000 tracers (initially distributed uniformly over the straight intervals $y = 0.408$, $x = -0.93 - 0$, or $x = -0.32 - 0$) in their initial positions were computed to illustrate the intricate behavior of the system. The plots shown there illustrate a strong instability of trajectories with respect to their initial positions. Their fractal properties resemble those described in Section 3.2 in the framework of a simple kinematic model.

The geophysical significance of the model considered can be seen by specifying the control parameters in a dimensional form. If the basin radius is $a = 500$ km (about half the width of the Sea of Japan) and the smallest width of the free current is 100 km, then $y_1 = 0.2$ and $\sigma_0 = 0.081632$. If the debit of the incident current is taken to be 1 Sv (Sverdrup) $= 10^6$ m^3 s^{-1} and if the current is assumed to encompass a layer 100 m thick in the vertical, then we obtain $q = 10^8$ cm^2 s^{-1} in the barotropic case, the value determining the velocity scale $U^* = q/\pi a \sigma_0 \approx 8$ cm s^{-1} and the time scale $t^* = aU^* \approx$ 72 days. It follows from relation (39) that

$$\beta = 8U^* a^2 = 2.56 \times 10^{-14}\ (\text{cm s})^{-1} \geqslant 4.68 \times 10^{-16}\ (\text{cm s})^{-1} = \beta^*$$

(which corresponds to the latitude of the Tsugaru Strait). Therefore, the domination of the topographic beta effect over the planetary one is assured. All the estimates obtained are rather reasonable and it is expected that the models proposed may be useful in studying Far Eastern margin seas, which are known to have a high intraannual variability of mass fluxes through their straits.

5.3 Topographical vortices

It is known (see Ref. [71], monographs [72, 73], and the references therein to observations in the ocean) that topographic vorticies in the ocean (and the atmosphere) appear in fluid flows over localized bottom features (seamounts, hollows, ridges, and troughs) due to the conservation law of the potential vorticity on the rotating Earth. A quasi-steady anticyclonic vortex appears over a seamount and a cyclonic one over a hollow. Topographic vorticies provide ventilation of oceanic water masses and are able to trap planktonic larvae for a long time. As a result, the planktonic biomass in the vortex region is two orders of magnitude larger than its background value [73, 74]. The role of topographic vortices in the formation of cobalt – manganese crusts of guyots (seamounts with cut tops) and in a strong transverse asymmetry of sedimentation has been noted in Ref. [71]. The flows over Fieberling Guyot (32° 25′ N, 127° 75′ W), situated in the Pacific Ocean at the distance about 1000 km from the south Californian coast, have been especially well studied. The horizontal scale of the guyot is approximately 40 km, the height is ≈ 3.5 km, and the ocean depth is ≈ 4 km. Direct hydrographic measurements (see [76] and the references therein) have revealed quasi-steady anticyclonic circulation over the guyot, a wide background flow with velocities $0.1 - 0.2$ m s^{-1}, and a strong tidal current with velocities 0.14 m s^{-1} (for a tide with the period 23.93 h) and about 0.7 m s^{-1} (for a tide with the period 25.82 h). The velocity of the background tidal current is ten times smaller. Maximum mean current velocities occurred at a height about 50 m above the seamount surface. Mixing near the guyot was estimated to be an order of magnitude greater than the typical values for the ocean interior.

We briefly mention other examples of interaction between oceanic eddies and currents. Individual large-scale eddies (with diameters of the order of a few dozen kilometers) can separate from the main stream of the meandering Kuroshio and the Gulf Stream. The unsteadiness of real currents and eddies is due to variations in their velocities, circulation, and sizes in a wide frequency range. Western boundary currents with mesoscale eddies to their east are common in different parts of the World Ocean. We mention (see [77] and the references therein) the well-studied deep-water western boundary current in the North Atlantic with mean velocities of the order of $0.05 - 0.1$ m s^{-1}, whose waters are trapped for a while by deep-water mesoscale cyclonic eddies. The well-known surface eddies near the Kuroshio and the Gulf Stream interact with western boundary surface currents. In shallow seas and bays, large-scale eddies are generated due to the wind and irregular bottom topography. Tidal currents cause periodic perturbations, which, as is shown below, are responsible for the intricate and inhomogeneous mixing of water masses.

The incident-flow nonvortical components of background currents developed in boundary regions nevertheless have deformation properties. This feature can be removed by considering the flow on an unbounded plane. For example, in the simplest case of an unbounded f plane (the Coriolis parameter is $f = f_0 = \text{const}$) with the topographic bottom evaluation $h(x, y)$, we have the topographical vorticity

$$\omega = -\frac{f_0}{H}\, h\,. \tag{51}$$

The only incident flow bounded on the entire plane is a spatially uniform flow $W(t)$ directed at an angle $\theta(t)$ to the x-axis. The corresponding streamfunction is

$$\psi_2 = W(x \cos\theta - y \sin\theta)\,, \qquad W > 0\,. \tag{52}$$

Although the vortical part of the streamfunction ψ_1 is formally obtained as a convolution of the right-hand side of Eqn (51) with the Green's function for the Laplace operator, it is possible to obtain corresponding quadratures only for a limited set of model bottom-relief shapes. The simplest shape is an axially symmetric $h(r)$, $r^2 = x^2 + y^2$. The topographical flow in this case is a circular vortex with the azimuthal velocity $V(r) = \mathrm{d}\psi_1/\mathrm{d}r$ related to the vorticity by the Stokes formula

$$rV = \int_0^r \omega(\rho)\,\rho\,\mathrm{d}\rho = -\frac{f_0}{2\pi H}\,\tau(r)\,, \tag{53}$$

where $\tau(r) = 2\pi \int_0^r h(\rho)\,\rho\,\mathrm{d}\rho$ is the volume of a bottom elevation chosen in the form of a cylinder with radius r. From the Stokes formula, we have the asymptotic formulas

$$V = \begin{cases} \Omega r\,, & r \to 0\,, \\ \dfrac{\Gamma}{2\pi r}\,, & r \to \infty\,, \end{cases} \tag{54}$$

corresponding to solid body rotation with the angular velocity $\Omega = -f_0 h(0)/2H$ in the neighborhood of the vortex axis and to the velocity field of a point vortex with the circulation $\Gamma = -f_0 \tau_\infty / H$ at a large distance from the vortex center, where $\tau_\infty = \tau(\infty)$ is the total elevation volume. The above asymptotic formulas coincide [at $\tau_\infty = \pi a^2 h(0)$] with the corresponding parts of a piecewise analytic solution for a circular cylinder of the height $h(0)$ and radius a. The case with an incident flow of type (53) was recently studied in Ref. [78] without analysis of chaotic mixing.

A piecewise analytic velocity field with a discontinuity of the vorticity at the boundary of the bottom elevation complicates numerical integration of the equations for trajectories intersecting the cylinder boundary. These difficulties can be easily avoided by specifying any analytic relief in (53) qualitatively representing the main features of localized elevations. Asymptotic expressions (54) guarantee the existence of a point $r = L^*$ at which $V'(L^*) = 0$. Using characteristic scales of length L^*, velocity V^*, time $t^* = L^*/V^*$, streamfunction $\psi^* = V^* L^*$, and bottom elevation $h^* = h(0)$ and introducing dimensionless variables instead of (53), we obtain

$$rV = -\sigma \int_0^r h(\rho)\, \rho \, \mathrm{d}\rho \,, \qquad (55)$$

where we introduce the topographic parameter $\sigma = h^*/H\,\mathrm{Ro}$ and the Rossby number $\mathrm{Ro} = V^*/f_0 L^* = 1/f_0 t^*$. The quasi-geostrophic approximation requires the condition $h^*/H = O(\mathrm{Ro})$ to be satisfied, i.e., $\sigma = O(1)$ [78]. Moreover, it is evident that

$$\left.\frac{\mathrm{d}V}{\mathrm{d}r}\right|_{r=1} = 0 \,, \qquad (56)$$

i.e., the distance from the center at which azimuthal velocity reaches its extreme value determines the horizontal scale.

We consider a seamount of the Gaussian shape $h(r) = \exp(-\alpha r^2)$, where $\alpha > 0$. From (55), we have

$$V = \frac{\sigma}{2\alpha r}\left(\exp(-\alpha r^2) - 1\right), \qquad (57)$$

whence using (56) we find $\alpha \approx 1.256$ as the single positive root of the equation $1 + 2\alpha = \exp \alpha$ and

$$V_{\mathrm{m}} = V(1) = -\sigma(1 + 2\alpha) \approx -0.3285\,\sigma \,.$$

The azimuthal velocity distribution of form (56) with $\sigma < 0$ has been used in laboratory simulation of cyclonic vortices in Ref. [79]. Figure 13 shows a radial profile of velocity (57), where $R_{\mathrm{e}}(V)$ and $R_{\mathrm{h}}(V)$ denote two branches of the function inverse to $V = V(r)$. It is possible to obtain many other analytic shapes of bottom relief with asymptotic behavior (54) required. For example, in the case of the algebraic dependence $h(r) = 1/(1 + r^2)^2$, we find the following expressions for azimuthal velocity and streamfunction from (55) under condition (56):

$$V = -\frac{\sigma}{2}\,\frac{r}{1 + r^2}\,, \qquad \psi_1 = -\frac{\sigma}{4}\ln(1 + r^2)\,, \qquad (58)$$

where $V_{\mathrm{m}} = -\sigma/4$. In our case, Eqn (49) for linear stability reduces to an equation that is independent of the incident velocity relation,

$$d = -\frac{1}{2r}(V^2)' \,. \qquad (59)$$

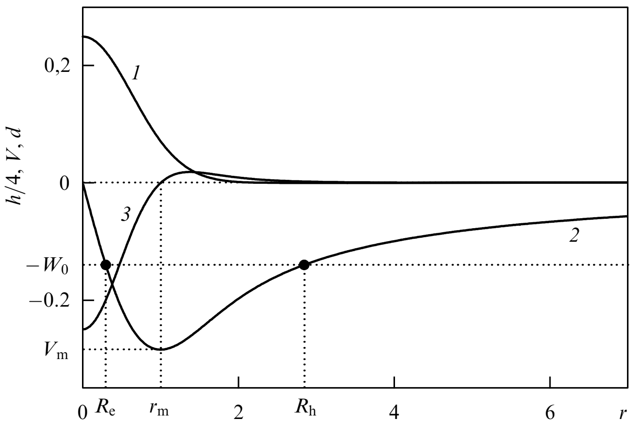

Figure 13. Radial distributions of bottom elevation (curve *1*), of the azimuthal topographic velocity (curve *2*), and of the stability indicator (curve *3*) for a seamount of a Gaussian shape.

For (57), this implies stability over a seamount ($r < 1$) and instability outside of this domain ($r > 1$). The dependence $d(r)$ for (57) is also shown in Fig. 13, where r_{m} is the position of the azimuthal velocity maximum and W_0 is the stationary value of the incident current.

For a steady incident current $W = W_0 = \mathrm{const}$, it is convenient to assume $\theta = 0$. There are no critical points in the total flow if $W + V_{\mathrm{m}} > 0$, whereas there are two points, elliptic $(0, -R_{\mathrm{e}}(-W))$ and hyperbolic $(0, -R_{\mathrm{h}}(-W))$, if $W + V_{\mathrm{m}} < 0$. A separatrix intersecting itself at the hyperbolic point divides the flow region into two parts: that with closed streamlines surrounding the elliptic point inside a homoclinic loop and that with unbounded trajectories outside it. In the nonstationary case, an instant picture of streamlines, which no longer coincide with particle trajectories, can be obtained for a given W and θ by simple rotation by the angle θ. Moreover, both critical points describe the given parametric curves

$$x_{\mathrm{e,h}} = R_{\mathrm{e,h}}(-W)\sin\theta \,, \qquad y_{\mathrm{e,h}} = -R_{\mathrm{e,h}}(-W)\cos\theta \,. \qquad (60)$$

The homoclinic tangle under consideration is a typical structurally unstable picture (see Fig. 2). Its perturbation in the form of harmonic oscillations of W breaks the topological equivalence of the corresponding maps and produces chaotic effects. Deterministic chaos in dynamical systems of the type mentioned above has been well studied in various models in the natural sciences, including hydrodynamic problems. For example, in classical hydrodynamics [80], the model with an incident flow washing a cylinder produces an instant picture of streamlines with a homoclinic separatrix loop, which is a precursor of arising chaotic mixing under perturbations [2]. A similar problem with a cylinder degenerated into a point-like vortex has been studied by the perturbation method in Ref. [81] with the aim of estimating the width of a stochastic layer. A detailed topological analysis of chaotic scattering in the model with a fixed-point vortex was given in Section 3.

In our case, we consider the simplest unidirectional oscillating flow as an incident current

$$W = W_0\left[1 + \varepsilon \sin(\nu t + \varphi)\right], \qquad \theta = 0 \,. \qquad (61)$$

Using the standard Melnikov technique to estimate the width of a stochastic layer [2, 19, 82, 83], it can be shown [84] that the

Melnikov integral has at least one maximum with respect to the frequency ν. Numerical simulation that involves computing scattering diagrams and estimating the number of particles reaching a fixed line has shown [84] that the maximum washing out occurs at the frequency close to the value $\nu = 0.25$. A prominent feature is the initial increase in the washing out rate with increasing the frequency and a rather slow rate of approaching the regime where particles barely leave the vortex region. A typical picture of the chaotic character and destruction of the vortex core was presented in Ref. [84]. Metamorphoses of similar pictures depending on the frequency ν have been presented in Ref. [84], where one can also find a collection of Poincaré cross sections for the optimal frequency $\nu = 0.25$ and a set of values of the perturbation amplitudes ε in the range $[0-0.6]$. As the perturbation amplitude increases, the vortex core with regular trajectories shrinks, individual vortices (islands) around it are destroyed, and an area with chaotic mixing, from which particles are carried out into a free-flow region, expands.

The mixing and transport of passive scalars in this problem are determined by a chaotic invariant set Λ of the same type as in the basic model for chaotic advection in Section 3. The set consists of unstable periodic orbits with all possible periods and aperiodic orbits with stable (Λ_s) and unstable (Λ_u) manifolds. Along trajectories from Λ_s, particles from an incident flow in the phase space come into the vortex core and remain there forever. Trajectories of particles close to Λ_s remain in the vortex core near trajectories from Λ for a long time, moving along the unstable manifold Λ_u.

The important quantitative characteristic of the divergence of initially close trajectories is the Lyapunov exponent, which can be calculated in a finite time interval using a simple algorithm [84] proposed in Ref. [66]. Useful information is also provided by the 'Lyapunov time,' which is the quantity that is inverse to the corresponding Lyapunov exponent [85]. Comparison of distributions of the quantities mentioned above [84] allows distinguishing regions from which tracers are not washed out but rotate in the vortex region. Regions from which tracers are not washed out up to a certain time and those specified by certain values of the Lyapunov time correlate with each other. This fact confirms once more [67] that the time of residence in the vortex region is an adequate characteristic of chaos in open dynamical systems of the considered type. The relation between the residence and Lyapunov times, which are close, on average, to a quadratic one, has been found for the optimal frequency $\nu = 0.25$ [85].

A variety of shapes of possible bottom elevations, the existence of boundaries with given values of nonstationary and balanced debits determining the character of an incident flow are the factors that generate different classes of problems with chaotic properties.

The anisotropic geometry of a localized bottom elevation on the unbounded f-plane was taken into account in paper [86], where a separation of variables in the Poisson equation for a topographic component of the streamfunction in elliptic coordinates (p, q) was used:

$$\begin{aligned} x &= \rho \sin p \cosh q\,, \qquad 0 \leqslant p \leqslant 2\pi\,, \\ y &= \rho \cos p \sinh q\,, \qquad 0 \leqslant q < \infty\,, \\ \rho &= \mathrm{const}\,. \end{aligned} \tag{62}$$

The shape of a seamount is modeled by the function

$$h(q) = \frac{1}{1 + (\gamma \sinh 2q)^{2m}}\,, \tag{63}$$

where m is assumed even for simplicity. The incoming flow has form (52) at a constant value of the angle θ. Specifying the angle, it is possible to consider variants of a longitudinal ($\theta = 0$) and a transversal ($\theta = \pi/2$) flow over an obstacle with elliptic isobaths. In numerical experiments, the values $\rho = 2$, $\gamma = 1$, $m = 6$, $\sigma = 0.5$, and $W_0 = 0.2$ were used (the transformation to dimensionless variables was the same as in the axially symmetric case). The bottom relief and the corresponding topographic velocity profiles in the main sections of a family of elliptic isobaths at $x = 0$ and $y = 0$ are analogous to those presented in Ref. [86] (see Fig. 3 in that paper). Pictures of distributions of critical points in the total flow and positions of the lines of linear neutral stability and of a separatrix are topologically the same as in the axially symmetric case, but are different in the cases of longitudinal and transversal flows. Comparing time dependences of the number of particles washed out from the vortex region for n periods of the oscillating (with the frequency ν) flow (61), it has been shown that the optimal washing out was realized at the frequency close to $\nu = 0.2$. Moreover, a ventilation of the vortex region is more effective in the case of the transversal flow. Poincaré cross sections computed for longitudinal and transversal flows [86] have shown that the vortex region, filled up densely with regular trajectories, breaks with increasing the frequency ν. Moreover, this occurs under the influence of two competing mechanisms: the appearance of a stochastic layer near the unperturbed separatrix and resonances in the vortex core leading to the generation of new elliptic and hyperbolic points. In comparison with the axially symmetric case, the transport of tracers in the elliptic case is more effective (with compatible values of the control parameters), and the optimal frequency varies depending on the shape of a seamount and its orientation.

The authors of [86] attempted to apply the technique of 'lobe dynamics' [83] for analyzing the initial phase of the process of chaotization using the numerical algorithm proposed in [87]. However, the algorithm was not fully realized, and the Poincaré cross section technique was used to estimate the effect of washing out the particles.

5.4 Model with a coastal line

Because Eqns (25) are linear, it is easy to find a solution on the plane where the condition for the absence of leakage on the straight boundary $y = 0$ is satisfied using the method of mirror mapping. For example, a dimensionless streamfunction for a delta-like topographic perturbation at the point $(0, 1)$, placed in a uniform flow with the velocity $W(t)$ directed along a boundary, has the form

$$\psi = -W(t) y + \sigma \ln \frac{x^2 + (y+1)^2}{x^2 + (y-1)^2}\,. \tag{64}$$

In the stationary case $W = W_0 = \mathrm{const}$, streamlines with different values of $W_0 > 0$ (the critical value is $W_0 = 4$) are plotted in Fig. 14. As the value W_0 decreases, the separatrix changes its form from a homoclinic ($W_0 = 4.4$) to a heteroclinic one ($W_0 = 3{,}6$). Following Ref. [81], an asymptotic analysis of the width of a stochastic layer, based on simple physical considerations, has been carried out in

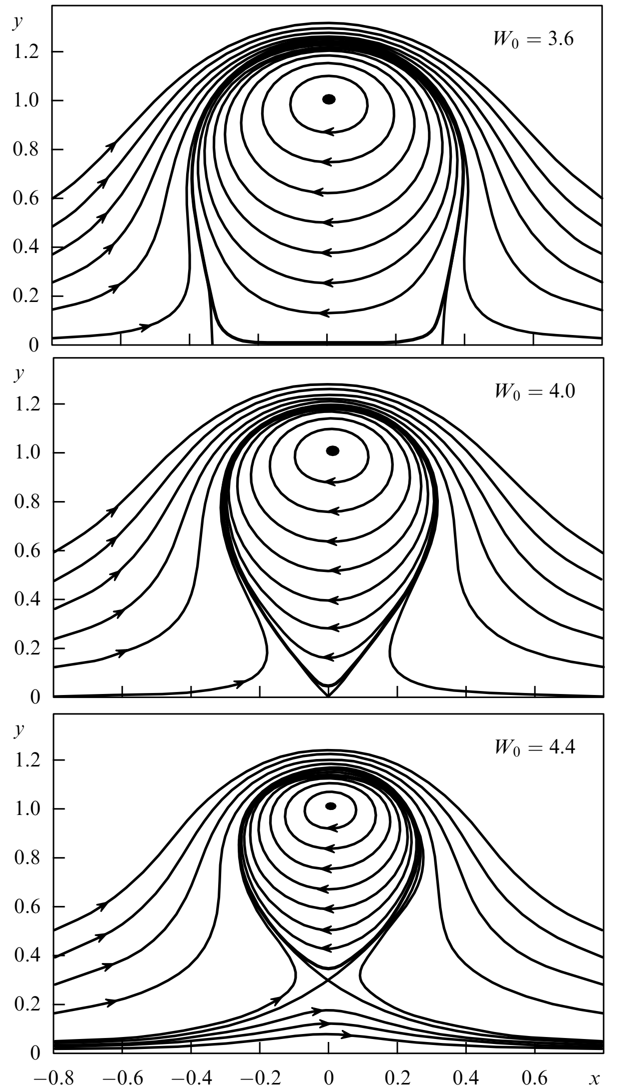

Figure14. Streamlines in the stationary case.

Ref. [88]. It has been shown there that the presence of a boundary near a topographic vortex increases the width of the stochastic layer. With characteristic values of the parameters in Ref. [81], the stochastic layer increases in the presence of a boundary half as much again and may occupy a significant part of the vortex region.

Stable and unstable manifolds of a chaotic invariant set determine the washing out of particles from the vortex region; the process evolves in accordance with the scenario described in detail in Section 3. The topological and fractal properties of trajectories belonging to this set change with the increasing influence of the boundary (with a change in the values of W_0). Nevertheless, there is an infinite variety of unstable periodic orbits with all possible values of the period, weakly chaotic trajectories, sticking to islands of regular motion, and chaotic trajectories with a wide range of values of the residence time in the vortex region. To quantitatively characterize the behavior of trajectories, the time of their trapping in the vortex region and the corresponding Lyapunov exponent accumulated for that time were used in Ref. [89]. Both characteristics were calculated for all the phase portraits shown in Fig. 14. The distribution of the accumulated Lyapunov exponents corresponding to the initial particle positions allows distinguishing the basic types of trajectories. Regions with small values of the Lyapunov exponent are situated in the vortex core and inside regular-motion islands immersed in a chaotic sea. Regions with larger values of the Lyapunov exponent and smaller values of the trapping time are situated near the unperturbed separatrix. The corresponding initial positions are near the unstable manifold of the chaotic invariant set. The trajectories with intermediate values of the Lyapunov exponent and long trapping times of particles in the vortex region are close to the stable manifold. In the case of strong influence of the boundary ($W_0 = 3.6$), it has been found that regions with chaotic motion specified by a distribution of the accumulated Lyapunov exponents and those specified by a distribution of the particle trapping times may be different.

The difference mentioned above can be explained by the presence of trajectories of a special type that are very rare in the case of weak influence of the boundary and in its absence [89]. These trajectories are distributed over almost the entire vortex region. They have large values of the accumulated Lyapunov exponent but do not escape from the vortex region for a long time. Among them can be trajectories tracking for periodic orbits with large periods and periodic saddle orbits as well as wandering chaotic trajectories sticking to the boundaries of regular motion islands. However, their prominent feature is frequent 'jumps' between the attracting objects (possibly of different types) and low probability of escaping from the vortex region. This kind of behavior is typical of Hamiltonian systems with bounded phase space. The presence of such trajectories in our model may be explained by the appearance of a large number of cantori, close to KAM tori, as a result of changes in the phase space topology. In this case, percolation of a particle through a cantorus is still more or less probable, but it can percolate through neighboring cantori, ending up in either the vortex core or the free-current region. Thus, the probability of a particle going through a few cantori and exiting to the free-current region is rather small. To identify trajectories with such a behavior, the combined criterion was proposed in Ref. [90]:

$$\alpha = \frac{t}{T} \frac{\lambda}{\lambda^*} \frac{dy}{r} , \qquad (65)$$

where T is the time instant when most particles escape from the vortex region, λ^* is the accumulated Lyapunov exponent averaged over all trajectories, dy is the maximum distance between successive intersections of the y axis (for $y < 1$), and r is the distance between the elliptic and hyperbolic points. Figure 15 shows the distributions of α corresponding to initial tracer positions for three characteristic values of the velocity (see Fig. 14) and the case without the boundary ($W_0 = 2.0$). It is evident from Fig. 15 that as the influence of the boundary increases, the number of particles with large values of α also increases. The inequality $\alpha^* < \alpha$ (where α^* is the maximum value in the case of weak influence of the boundary) may be used as a criterion for distinguishing tracers of that type. It is important that the initial positions of those tracers be distributed irregularly over the vortex core. Their number can be estimated by computing those having a value of α larger than the given one (Fig. 16). We see that their number is $7-10\%$ at $W_0 = 4.0$ and 25% at $W_0 = 3.6$.

We conclude that on the one hand, the influence of the boundary increases mixing in the system, but on the other hand, it makes the fast escape of particles difficult, which seems to be related to the increasing number of islands of

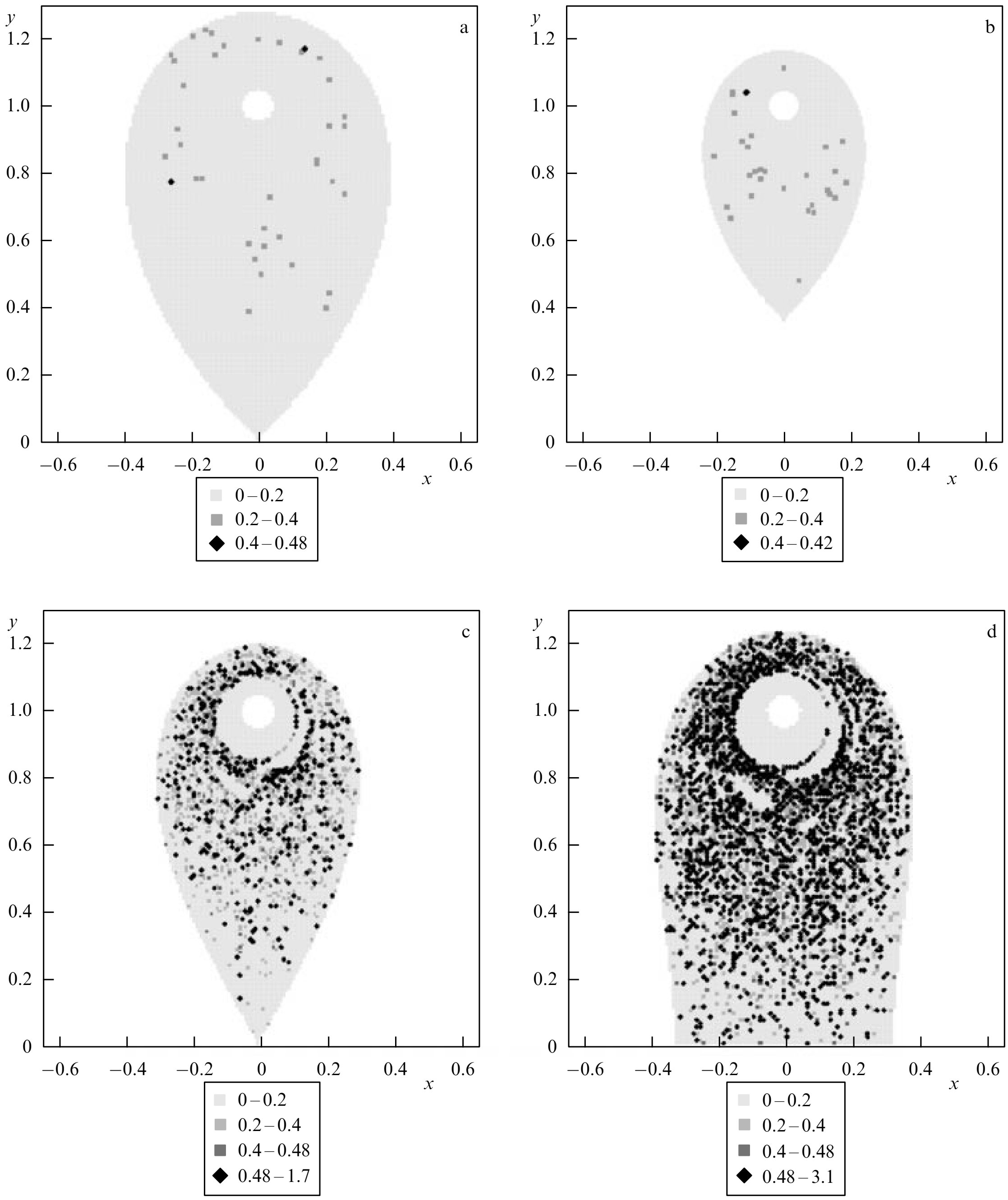

Figure 15. Distribution of the quantity α corresponding to initial tracer positions: (a) $W_0 = 2.0$, (b) $W_0 = 4.6$, (c) $W_0 = 4.9$, and (d) $W_0 = 3.6$.

regular motion or, more exactly, almost broken nonlinear resonances.

5.5 Two-layer model

We have considered barotropic dynamically consistent models for vortex motion in the ocean allowing chaotic advection [4, 84, 86, 90, 91]. But the real ocean is not uniform in depth. Therefore, investigation of chaotic advection in a baroclinic ocean seems to be a natural direction of constructing more complicated models. In the framework of the concept of background currents [4, 52], it is possible to formulate a dynamically consistent two-layer model of the ocean allowing chaotic mixing in the field of a point-like topographic vortex and nonstationary incident current. The motion of point-like vortices in a baroclinic ocean has been studied in the framework of such models [91], but the effects of chaotic transport have not been considered.

We consider a two-layer oceanic model in the quasi-geostrophic approximation in an unbounded basin. Streamfunctions of the background current generated by the interaction between a δ-like perturbation of the bottom relief $h(x, y) = \tau_\infty \delta(x, y)$ and an incident current (which is assumed to be barotropic), are solutions of Eqns (36) and (37). In the upper and lower layers, they have the respective form [4, 52]

$$\psi_1 = -Uy - \frac{f_0 \tau_\infty}{2\pi H} \left[\ln kr + K_0(kr) \right], \tag{66}$$

$$\psi_2 = -Uy - \frac{f_0 \tau_\infty}{2\pi H} \left[\ln kr - \frac{H_1}{H_2} K_0(kr) \right], \tag{67}$$

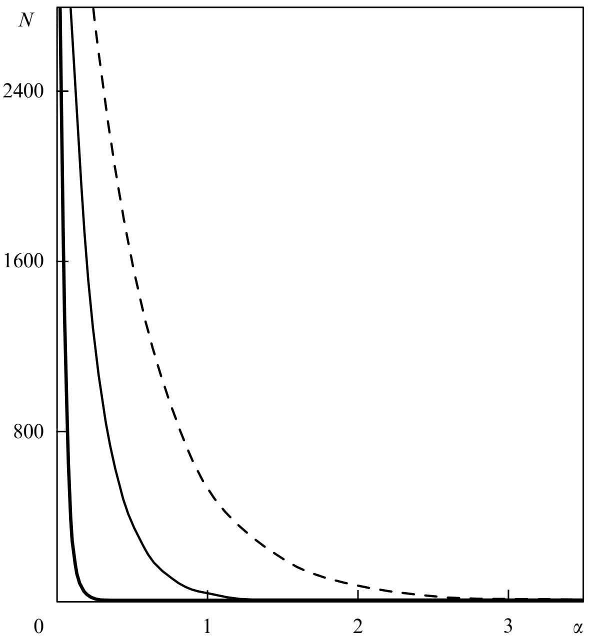

Figure 16. The number of tracers with α that are larger than a given one. The dashed line corresponds to the value $W_0 = 3.6$, the solid thin line to $W_0 = 4.0$, and the solid thick line to $W_0 = 4.6$.

where $r = \sqrt{x^2 + y^2}$, $K_0(kr)$ is the Macdonald function of the zeroth order, H is the depth, H_1 and H_2 are the thicknesses of the layers, U^* is a velocity scale, $h^* = h(0)$ is the effective elevation of the bottom,

$$L_\mathrm{d} = k^{-1} = \sqrt{\frac{g' H_1 H_2}{H f_0^2}}$$

is a linear scale, and $\tau_\infty = \pi h^* L^{*2}$ is the effective volume of the seamount. Choosing a scale for the streamfunction $\Psi = U^* L_\mathrm{d}$ and using the Rossby number $\varepsilon = U^*/(L_\mathrm{d} f_0)$ and the parameter

$$\sigma = \frac{f_0 L_\mathrm{d}}{U^*} \left(\frac{L^*}{L_\mathrm{d}}\right)^2 \frac{h^*}{H} = \frac{h^*}{\varepsilon H} \left(\frac{L^*}{L_\mathrm{d}}\right)^2$$

as dimensionless parameters, we pass to dimensionless variables denoted by primes,

$$\begin{aligned} &k(x, y) = (x', y')\,, \\ &(u, v, U) = U^*(u', v', W)\,, \\ &\psi = \Psi \psi'. \end{aligned} \tag{68}$$

Omitting the primes, we obtain

$$\psi_1 = -Wy - \sigma\big(\ln r + K_0(r)\big)\,, \tag{69}$$

$$\psi_2 = -Wy - \sigma\left(\ln r - \frac{H_1}{H_2}\, K_0(r)\right). \tag{70}$$

The constraint $\varepsilon \sim o(1)$, $\sigma \sim O(1)$ must be specified in the quasi-geostrophic approximation. Specifying $H = 4$ km, $H_1 = 900$ m, $H_2 = 3100$ m, $f_0 = 10^{-4}$ s^{-1}, $U^* = 10$ cm s^{-1}, $h^* = 310$ m, we obtain $L_\mathrm{d} = 1/k = 53$ km, $L^* = 31.8$ km, $\Psi = 5300$ m^2 s^{-1}, $\varepsilon \approx 0.0189$, and $\sigma \approx 1.0$, and hence the quasi-geostrophic approximation is satisfied.

According to (69) and (70), the equations of motion of fluid particles in the upper and lower layers have the form

$$\begin{aligned} u_1 &= -\frac{\partial \psi_1}{\partial y} = W + \frac{y}{r}\left(\frac{1}{r} - K_1(r)\right), \\ v_1 &= \frac{\partial \psi_1}{\partial x} = -\frac{x}{r}\left(\frac{1}{r} - K_1(r)\right), \end{aligned} \tag{71}$$

$$\begin{aligned} u_2 &= -\frac{\partial \psi_2}{\partial y} = W + \frac{y}{r}\left(\frac{1}{r} + \frac{H_1}{H_2}\, K_1(r)\right), \\ v_2 &= \frac{\partial \psi_2}{\partial x} = -\frac{x}{r}\left(\frac{1}{r} + \frac{H_1}{H_2}\, K_1(r)\right). \end{aligned} \tag{72}$$

Because the behavior of particles in the lower layer is virtually identical to that in the barotropic case, we consider only the upper layer. It is known from earlier studies of chaotic advection that the transport of fluid particles from the vortex region to the free-flow region is possible under a small nonstationary perturbation of the incident flow in velocity field (56). Parameters of the perturbation (frequency, amplitude, and phase) significantly influence the degree of this transport. To study the influence of the perturbation frequency on the tracer transport, numerical experiments with different values of these frequencies were performed with a patch of 8250 tracers initially filling the entire vortex region. The velocity of the incident flow was specified as

$$W(t) = 0.3\big(1 + 0.1 \sin(\nu t)\big)\,, \tag{73}$$

where ν is the perturbation frequency. The tracer was considered washed out if its trajectory crossed the control line $|x| = 3$ [91]. In Fig. 17, we show the dependence of the normalized number of tracers $N(\nu)$ escaped from the vortex region on the perturbation frequency. Along with the presence of the optimal perturbation frequency $\nu = 0.59$ [84, 92] at which the maximum number of tracers is washed out, there are also a few local extrema. Such behavior of $N(\nu)$ was not observed in any of the previous models [89, 92]. We note that because of large computation expenses, not all local extrema have been found.

5.6 Optimal frequency

The degree of chaotization of the system depending on the perturbation frequency has been studied in many works. In particular, it was shown that at high frequencies, the width of a stochastic layer is exponentially small [84, 92, 93]. It is reasonable to hypothesize [84, 92] that there should exist frequency values that are optimal for chaotic mixing. We consider three models for which frequency dependences of the chaotization degree of the phase space were obtained in Refs [86, 94] and explain the dependences based the analysis of the rotation time of particles along unperturbed trajectories around an elliptic point.

Because the systems under consideration, in contrast, e.g., to the system discussed in Ref. [95], are open, the task of measuring a chaotic component in the phase space is simplified. Indeed, irregular trajectories originally located in the vortex region leave it in the course of time, whereas regular trajectories remain within it [86]. Thus, uniformly placing a sufficient number of tracers in the vortex region and computing the fraction of tracers that leave the region for a long time, we obtain the fraction of chaotic trajectories among all the chosen ones, which can serve as a good

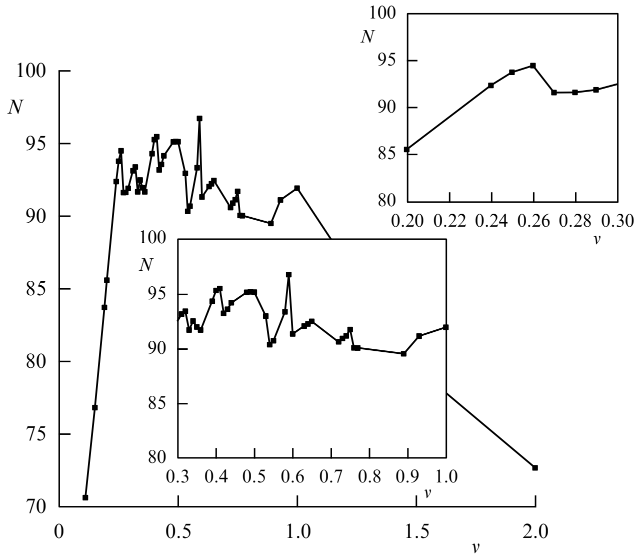

Figure 17. Perturbation-frequency dependence of the limit fraction of washed out tracers (the two-layer model).

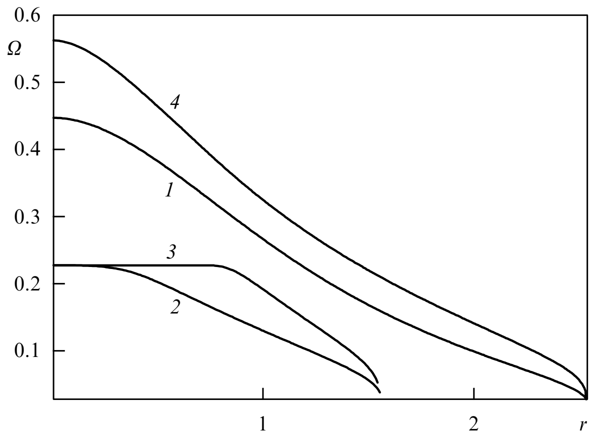

Figure 18. Dependence of the fluid-particle rotation frequency on the distance from the elliptic point along the line connecting the elliptic and hyperbolic points. The Gaussian (curve *1*), elliptic at $\theta = 0$ (curve *2*), elliptic at $\theta = \pi/2$ (curve *3*), and two-layer (curve *4*) models.

estimate for the measure of the chaotic component in phase space. In Ref. [86], the time dependences of the number of washed out tracers have been computed for different values of the perturbation frequency. Based on the analysis of stationary values of this quantity, it was hypothesized that an optimal frequency for chaotic mixing must exist, and the values of this frequency were computed with Gaussian and elliptic elevations. Figure 17 shows the dependence of the chaotization degree in the phase space (the fraction of tracers washed out from the vortex region) at the perturbation frequency for the two-layer model. Similar dependences were presented in Ref. [86] for models with Gaussian and elliptic seamounts, and more exact ones were shown in Ref. [96]. We note that these curves are plotted over a wider frequency range and with a better frequency resolution. This enables revealing local maxima and minima in one-layer models as well, although they are not so clearly pronounced as those in two-layer models [96].

Figure 18 presents the dependences of the rotation frequency in the unperturbed case ($\varepsilon = 0$) on the initial position of the trajectory taken on the y axis below the elliptic point. From the curves shown in Fig. 18, we can determine the initial position of the trajectories corresponding to nonlinear resonances of different multiplicities [93, 97]. An important feature of these curves is that not all simple nonlinear resonances can exist in the dynamical systems under consideration.

In accordance with the KAM theorem, at a perturbation frequency ν (under the condition that this frequency is possible in the system under consideration), nonlinear resonances are possible near the rotation frequency $\bar{\nu} = (n/m)\nu$, where n and m are integers. In the case of a Gaussian seamount, the resonance $\bar{\nu} = \nu$ cannot exist at perturbation frequencies $\nu > 0.44$. The rather simple resonance, closest to the elliptic point, is $\bar{\nu} = (4/5)\nu$ or $\bar{\nu} = (2/3)\nu$, and so on. A more accurate determination of the multiplicity of the nonlinear resonance closest to the vortex center requires a more detailed analysis. We suppose that there exists the following mechanism determining the chaotization degree in phase space. As long as the nonlinear resonance closest to the vortex center is located rather far from the center, it is overlapped by a subsequent resonance. In accordance with the resonance overlap criterion [93, 97], the stability islands determined by these resonances are destroyed, either totally or partially. As a result, trajectories are chaotic in the considered phase space region, and we have a local maximum of the chaotization degree in the phase space. With a further increase in the perturbation frequency, the width of the nonlinear resonance closest to the vortex center decreases because the rotation frequency of the corresponding trajectories are beyond the critical value (0.44 for a Gaussian seamount, 0.22 for an elliptic seamount, and 0.56 for the two-layer model) until this nonlinear resonance vanishes completely. As the width of the nonlinear resonance closest to the vortex center decreases, overlapping with the subsequent resonance also decreases. The destruction of the latter resonance ceases and one observes the formation or enlargement of the corresponding stability island, i.e., we have a local minimum of the chaotization degree in phase space. With a further increase in the perturbation frequency, the last nonlinear resonance remaining in the system approaches the center, simultaneously expanding in accordance with the estimate of the width of nonlinear resonance $\delta\bar{\nu} \sim \nu/m$ in Ref. [93]. Expansion of the two nonlinear resonances closest to the vortex center leads to an increase in their overlapping degree and, in accordance with the resonance overlap criterion, to the destruction of the corresponding stability islands, i.e., to an increase in the degree of chaotization in the phase space up to the attainment of a local maximum. After that, the subsequent resonance starts to disappear and the situation repeats. As the resonance with $n/m < 1$ approaches the vortex center, the resonance widths start to decrease with increasing m. Apparently, the global maximum of the chaotization degree in the phase space is located in the vicinity of the perturbation frequency that is critical for the model, i.e., the frequency at which the $n/m = 1$ resonance leaves the system. For a Gaussian seamount, elliptic seamounts with two orientations with respect to an incident current, and the two-layer model, the perturbation frequencies corresponding to local maxima of the chaotization degree in phase space and the related multiplicities of the

Table. Values of the perturbation frequencies corresponding to local maxima in the fraction of tracers washed out from the vortex region for models with a Gaussian seamount, elliptic seamount, and two layers. Multiplicities of the nonlinear resonances for which these frequencies are critical are indicated.

Gaussian seamount		Elliptic seamount				Two-layer model	
		$\theta = 0$		$\theta = \pi/2$			
ν	$n/m \approx 0.44/\nu$	ν	$n/m \approx 0.2/\nu$	ν	$n/m \approx 0.22/\nu$	ν	$n/m \approx 0.52/\nu$
0.22	2			0.11	2/1	0.26	2
0.26	5/3					0.32	5/3
0.28	3/2					0.34	3/2
0.33	4/3	0.15	4/3	0.165	4/3	0.41	4/3
0.44	1	0.2	1	0.22	1	0.48	~ 1
						0.59	~ 1
		0.24	4/5	0.3	4/5	0.65	4/5
		0.27	3/4				
		0.29	2/3	0.33	2/3	0.76	2/3
		0.38	1/2	0.44	1/2	1	1

resonances that attain the critical value of the frequency are given in the table (see [86]).

In general, the values given in the table confirm the conclusion that the perturbation frequencies at which the degree of chaos in phase space attains its local and global minima are related to the maximum rotation frequency of fluid particles for the corresponding model. But the accuracy of determining the multiplicity of the nonlinear resonances closest to the vortex center is appreciably reduced when approaching the optimal frequency. Apparently, this is related to the fact that our speculations are based on the perturbation theory, because both the KAM theorem and the nonlinear resonance analysis are based on the assumption that the perturbation is small. In our case, the center of the vortex of the perturbed system is appreciably displaced with respect to the position of the elliptic point in the unperturbed system. This may cause a drift of the frequency of the nonlinear resonances closest to the vortex center and the critical frequency of its existence. An analysis of the Poincaré cross sections at optimal frequencies with decreasing the perturbation amplitude confirms this conclusion. In other words, we observe a drift of the frequency of a nonlinear resonance with increasing the perturbation amplitude.

Although the above estimates are rough, we can conclude with confidence that in the models considered, the measure of chaos in phase space is rather large within the perturbation frequency range from half to twice the critical frequency. The estimate of the position of local extrema in the vicinity of frequencies corresponding to the closeness of nonlinear resonances to the critical frequency can also be considered convincing.

6. Laboratory experiments on modeling geophysical chaotic advection

6.1 A current with gyres

In this section, we present the results of a laboratory experiment carried out at the Woods Hole Oceanographic Institution in 2002 [77] with the aim of mimicking the interaction between a deep western boundary current and its adjacent recirculation gyres, and discuss how they can be interpreted with the help of geometric structures found in the basic kinematical model of chaotic advection (see Section 3). The experimental device is a cylindrical tank with the diameter 42.5 cm, mean depth 20 cm, and a slopping bottom with the slope 0.15 from the north to the south. The tank rotates with the angular velocity $\Omega = 2$ rad s^{-1}. The lid at the water surface rotates at a differential rate $\Delta\Omega < 0$, producing a uniform anticyclonic surface stress curl. This results in a western boundary current (the velocity is of the order of $0.1-0.3$ cm s^{-1}) with two adjacent gyres. The main control parameter of the nonlinearity is the ratio of the Stommel boundary layer width to the inertial boundary layer width $\delta \simeq 8\sqrt{\Delta\Omega/\Omega}$ [77]. At $\delta \leqslant 1.1$, the flow is almost steady. Varying the lid rotation rate $\Omega(t) = \Delta\Omega_0(1 + A_{\rm osc}\sin 2\pi t/T_{\rm osc})$, it is possible to produce a time-periodic flow. Three methods were used for measuring and visualizing the horizontal circulation. A horizontal laser beam illuminated neutrally buoyant particles, and their tracks were recording by a digital camera. Direct velocity measurements were made using an image velocity meter with a spatial resolution of 1 cm. Visualization of the flow also involved the introduction of dye into the flow and its illumination and video recording.

Within the range $1.1 \leqslant \delta \leqslant 1.4$, the flow consists of two gyres, a northern one and a southern one, which are revealed as an ∞-like figure under injecting dye. In the steady flow, mixing of dye occurs due to molecular diffusion. Chaotic dye advection occurs under the periodic perturbation of the flow ($20 \leqslant T_{\rm osc} = 2\pi/\Delta\Omega \leqslant 131$ s). Figure 19 shows dye patterns with the following three different injection points: in the western boundary current (i.e., outside the unperturbed separatrix, Fig. 19a), at the edge of the southern gyre (i.e., just inside its internal edge, Fig. 19b), and well inside the southern gyre (Fig. 19c). The experiments were carried out at $\delta = 1.25$, $A_{\rm osc} = 0.05$, and $T_{\rm osc} = 131$ s [77]. In the first two cases, transport and mixing demonstrate prominent filaments, which evolve in both the southern gyre (where they are more visible because of injecting the dye near the southern gyre) and the northern gyre (north is to the left and west is downward in these figures). In the figure, we in fact see the evolution of the unstable manifold Λ because the dye is injected near the unperturbed ∞-like separatrix. When the dye is injected inside the southern gyre, it remains there for a long time because the KAM tori are barriers penetrable only by molecular diffusion.

We note a similarity in the tracks of numerical (see Fig. 4) and laboratory (Fig. 19b) experiments. In both cases, dye was injected near the corresponding unperturbed separatrices, and both tracks are images of the corresponding unstable manifolds. The difference is caused by the fact that the unperturbed separatrix of the model flow has a loop-like form and the model flow therefore has a single

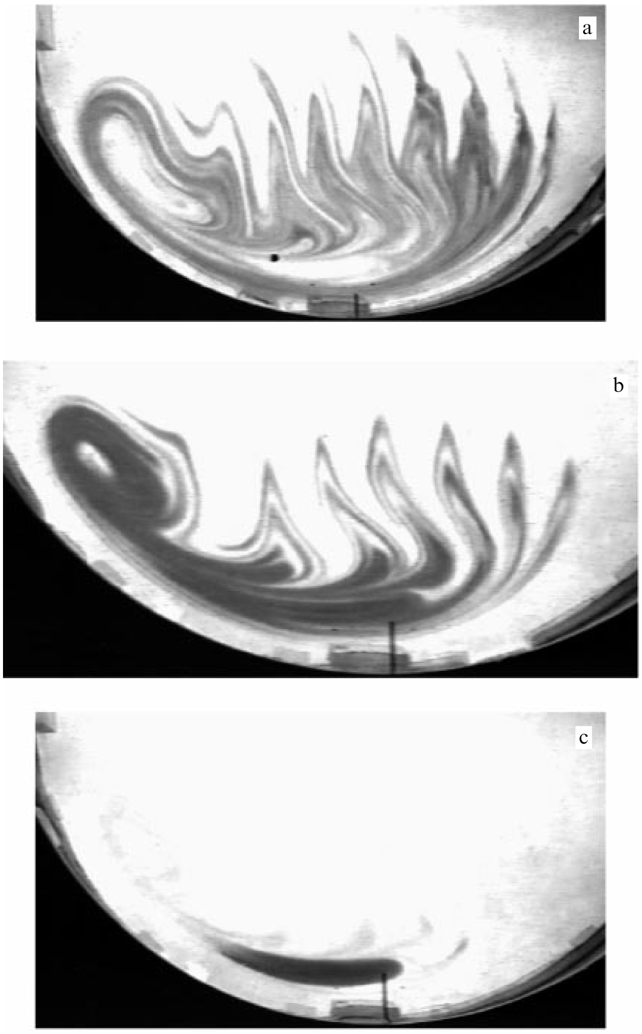

Figure 19. Dye patterns in the laboratory experiment [77] with injection (a) in the western boundary current, (b) just inside the edge of the southern gyre, and (c) well inside the southern gyre. Courtesy of L Pratt (Woods Hole Oceanographic Institution, Woods Hole, USA).

(southern) gyre. The geometric analysis of the fractal properties of the flow, transport, and mixing of passive scalars given in Section 3 can explain the main properties of chaotic advection in the laboratory experiment [77], which, as is stated by the authors of Ref. [77], can be considered a laboratory model for fluid mixing among western boundary currents and subbasin recirculation gyres.

6.2 A geostrophical jet with Rossby waves

In this section, we present results of laboratory experiments by H Swinney's group on chaotic advection of passive particles in a laboratory model of a quasi-geostrophic jet current with Rossby waves [98–100]. A tank with fluid, confined between two cylinders, rotates rapidly. The top and sides are transparent to allow recording dye particle trajectories with a video camera mounted on a rotating platform above the tank. A quasi-two-dimensional flow is forced by continuously pumping fluid in and out of the tank through holes in a sloped bottom (alternating sources and outlets, each of which consists of a large number of small-diameter holes). The sloped bottom mimics the beta-effect — a variation of the Coriolis force with the latitude. The pumping creates a radial pressure gradient, which, due to the Coriolis force, produces an azimuthal jet. The jet has a stable wavy shape in a wide range of the experimental parameters. Depending on the pumping force and the rotation velocity, two-dimensional currents with different wavenumbers or a different number of vortices are created. The azimuthal component of the velocity of the jet was two orders of magnitude larger than the mean radial velocity.

The measured radial dependence of the azimuthal component of the velocity for Reynolds numbers $\sim 10^4$ has the form of the Bickley jet $\operatorname{sech}^2\left[(r-\bar{r})/d\right]$, where $\bar{r}$ and d are, respectively, the measured values of the mean radius and width of the jet. Hence, the streamfunction should have the form of a hyperbolic tangent. Fourier transforms of the azimuthal component of the velocity indicate that there are two or more azimuthal modes. The simple streamfunction in polar coordinates was therefore assumed in Ref. [99] to be

$$\Psi = du_0 \sum_j \varepsilon_j \tanh \frac{r-\bar{r}-b\cos m_j(\theta-\omega_j t)}{d}\,. \tag{74}$$

It is similar to streamfunction (14) for the kinematic model of the meandering jet current. Here, $\sum \varepsilon_j = 1$, u_0 is the maximum possible velocity, ω_j is the azimuthal velocity of the jth wave with respect to the laboratory reference frame, and k_j is the wavenumber of the jth wave. In the reference frame rotating with a speed ω_1 (i.e., with the new set of polar coordinates r and $\varphi = \theta - \omega_1 t$), function (74) becomes

$$\Psi' = du_0 \left(\varepsilon_1 \tanh \frac{r-\bar{r}-b\cos m_1\varphi}{d} + \varepsilon_2 \tanh \frac{r-\bar{r}-b\cos m_2(\varphi-\delta\omega_2 t)}{d} + \ldots \right) - \omega_1 r^2\,, \tag{75}$$

where $\delta\omega_j = \omega_j - \omega_1$. It is evident that in the presence of only one wave ω_1, streamfunction (75) is stationary. With two or more waves, the equations of motion

$$\frac{\mathrm{d}r}{\mathrm{d}t} = -\frac{1}{r}\frac{\partial\Psi'}{\partial\varphi}\,, \qquad \frac{\mathrm{d}\varphi}{\mathrm{d}t} = \frac{\partial\Psi'}{\partial r} \tag{76}$$

are nonintegrable in general, and advection may be chaotic. We note that in contrast to the time dependence in the experiments in [77] (see Section 6.1) and other experiments on chaotic advection with periodic pumping [2], the time dependence in the present flow arises in a natural way due to the azimuthal waves.

The study of radial transport in the discussed experiments showed the presence of a barrier to mixing across the jet even with Reynolds numbers of $\sim 10^5$, for which the Eulerian velocity field was turbulent. Poincaré cross sections computed with nonlinear dynamical system (76) with streamfunction (75) demonstrated the existence of such a barrier with both two-wave and three-wave perturbations [99] at reasonable values of the parameter $b/d < 1$ (the experimental values are in the range $b/d \sim 0.5-0.6$). Variance is a measure of the azimuthal transport,

$$\begin{aligned} \sigma^2(t) &= \left\langle \Delta\theta^2(t,\tau) \right\rangle - \left\langle \Delta\theta(t,\tau) \right\rangle^2\,, \\ \Delta\theta(t,\tau) &= \theta(t+\tau) - \theta(\tau)\,, \end{aligned} \tag{77}$$

where the averaging is over time τ for individual trajectories and over different trajectories in the ensemble. Spreading of a dye patch in an inhomogeneous velocity field is possible due to spatial and temporal variations in the fluid velocity or molecular diffusion. Molecular diffusion is totally negligible on the time scale of the experiments. But in real experiments, technical noise and finite-size particle effects (neutrally buoyant tracers ~ 1 mm in diameter) deviate real trajectories from the corresponding theoretical ones.

The presence of coherent structures (jets and vortices) results in correlations in particle motion that can persist for long distances and/or times. This may result in the inapplicability of the central limit theorem and, therefore, in an anomalous diffusion $\sigma^2 \sim t^\gamma$, $\gamma \neq 1$ (see reviews on the anomalous diffusion [8, 101]). Both subdiffusion with $\gamma < 1$ and superdiffusion with $\gamma > 1$ are possible. Transport properties are very simple in the case of the stationary streamfunction in the moving frame. The azimuthal coordinate $\theta(t)$ of the particles in the vortex oscillates around a constant value and grows linearly in time for the particles in the jet. The breakup of some invariant curves in flows with periodic streamfunction (75) results in effects typical of Hamiltonian systems described in Section 3: 'stickiness' of trajectories to the boundaries of 'islands' in the phase space, fractals, Levy flights, anomalous transport, etc. These effects are due to the existence of the basic invariant sets in Hamiltonian systems (see Section 3). A typical chaotic trajectory in a nonhyperbolic Hamiltonian system demonstrates intermittency, i.e., its chaotic fragments alternate with regular ones. The regular fragments consist of events of two kinds: trapping of trajectories in dynamical traps ('stickiness'), easily identified in $\theta(t)$ records as small oscillations, and Levy flights with a steady azimuthal velocity represented by long diagonal straight lines on the graph $\theta(t)$.

Recording trajectories of a large number of particles (from 1300 to 1700), the authors of Ref. [102] stated the following properties of the probability distribution functions $P(t)$ for these events. The most representative results were obtained with a seven-vortex jet flow. The probability distribution function for the flight duration shows a clear power-law 'tail', $P_F(t) \sim t^{-\mu}$, where $\mu = 3.2 \pm 0.2$. This value is approximately the same for both clockwise and counterclockwise flights. The sticking probability distribution function does not show an exponential decay or a clear power-law 'tail.' The variance for an ensemble of tracers was measured to be $\sigma^2 \sim t^{1.5}$; a superdiffusion therefore occurs. We note that for $\mu > 3$, the central limit theorem predicts normal diffusion with $\sigma^2 \sim t^\gamma$, where $\gamma = 1$. Analogous measurement with a six-vortex periodic flow showed the magnitude $\mu = 2.5 \pm 0.2$ and superdiffusion with $\gamma = 1.65 \pm 0.15$.

Laboratory experiments in a two-layer rotating fluid were described in Ref. [103]. A sequence of period-doubling bifurcations were observed in Ref. [104] en route to baroclinic chaos. Theoretical and experimental works on chaotic behavior in unstable baroclinic systems were reviewed in Ref. [105]. Chaotic mixing and transport of passive particles in a quasi-two-dimensional four-vortex flow with a time-periodic dependence of the Eulerian velocity field were studied experimentally in Refs [106–108]. The experiments were performed in a thin layer of electrolyte where the flow was generated magnetohydrodynamically. A review of the stability of the vortex structures in quasi-two-dimensional shear flows was given in Ref. [109].

7. Conclusion

We have shown the fruitfulness of the ideas and methods of the theory of dynamical systems in describing Lagrangian transport and mixing in the ocean. We briefly mention some problems left beyond the scope of this review. Advection equations with fully deterministic right-hand sides are, of course, idealistic models of geophysical flows. Even numerical computation is subject to random errors. The smallness of errors in computing stable trajectories guarantees a reproducible result. In the case with unstable chaotic trajectories, an exponential increase in a small error rapidly leads to a departure of the computer trajectory from the theoretical deterministic one. This may seem to disavow any numerical computation of chaotic trajectories. But it is known that in strongly chaotic systems, there is always a chaotic deterministic orbit (i.e., without any noise) near any noisy orbit. This has been rigorously proved for maps with hyperbolic dynamics. We are therefore unable to exactly compute a theoretical chaotic orbit with a given initial point. Instead, we obtain a noisy computer orbit, which is a theoretical orbit for a close initial point. In J Ford's words: "Gods of chaos help us to compute uncomputable."

In modeling transport and mixing in real geophysical flows, it is necessary to take multi-scale turbulence into account. In the framework of the dynamical approach, a random velocity field with given statistical properties must be added to the right-hand side of the advection equations. With kinematic models, the respective streamfunction can be written as a sum with a large number of harmonics with random phases within a given frequency range. In papers [25, 27, 110], it has been shown for the chaotic advection model with a fixed point-like vortex in an unsteady incoming flow that some fractal and anomalous statistical properties of transport are persistent under small and moderate noise. Moreover, some properties of the Lyapunov stability of motion survive under a noisy perturbation. As a result, there arise the so-called coherent clusters in Hamiltonian systems with noise [110, 111], which are compact blobs of passive tracers advected coherently in noisy hydrodynamical incompressible flows for a long time (as compared with the temporal characteristics of the flow). This phenomenon occurs due to nonlinear resonances in Hamiltonian systems, in contrast to stochastic clusterization, which may occur in totally random velocity fields [112, 113].

Thus, there are three basic mechanisms of nonlinear transport. In the first, as a result of bifurcations, there arise hyperbolic (saddle) points with corresponding stable and unstable manifolds that strongly change the direction of transport in their neighborhoods. The second mechanism is caused by periodic or quasiperiodic perturbations (chaotic advection), and the third by random perturbations. If the Eckman transport, forced by wind, occurs only in the very upper layer of the ocean, then chaotic advection may be a dominant mechanism at large depths.

Chaotic advection is an effective mechanism of transport for plankton, larvae, and fry. Mathematical models for the processes of survival, death, and transport of biological phenomena are self-consistent sets of equations of advection, reaction, and diffusion [114]. The dynamical system approach in physical oceanography is not limited to problems of advection of passive particles. This approach may be used successfully and has already been used in studies of convective mixing and transport (for example, in thermohaline convection), advection of biologically and chemically active particles, and advection of finite-size tracers in viscous fluids. These tasks require methods of the theory not of Hamiltonian but of dissipative systems.

In physical oceanography, a problem is conventionally considered solved as soon as hydrodynamic equations of motion are solved. From the standpoint of the dynamical approach to the problems of transport and mixing, it is only a beginning. A Eulerian velocity field can be found experimentally or as a result of numerical integration of relatively complicated dynamically consistent models of flows. Then the corresponding data are substituted in the right-hand side of the advection equations for passive scalars (1). The discovery and investigation of the Lagrangian structures, barriers to transport, exit channels, and regions of intensive mixing provide valuable information about basic properties of transport and mixing of water masses in the ocean and atmosphere. But the velocity fields, which are input data in computing invariant Lagrangian manifolds, contain inevitable errors due to finite-size griding, uncertainties in initial conditions and parameters (for example, in a field of wind), and so on. How robust and stable (in the common sense) are the Lagrangian structures with respect to errors in a Eulerian velocity field, and how strongly do the Lagrangian and Eulerian errors correlate with each other? These questions are far from being answered yet. We mention paper [115], where they have been discussed.

Another problem is connected with the fact that a Eulerian velocity field, computed or measured, is not a dynamical system in the strict sense, but is a collection of numbers on a spatial and temporal grid. This field is known (with a finite accuracy) in a finite time interval and is therefore aperiodic. Mathematical notions in the theory of dynamical systems (invariant manifolds, fractals, sets, chaos, Lyapunov exponents, etc.) are defined in infinite time. Mathematicians have been able to generalize the basic notions in the theory of dynamical systems to finite times. Strictly speaking, the simple kinematic model considered in Section 3 is not chaotic because all trajectories of passive particles in an open flow are asymptotically regular. But we have shown that motion in the mixing region has all the signatures of authentic chaos with a homoclinic structure, fractals, a chaotic invariant set, and a positive Lyapunov exponent. Because infinite time is not a physical reality, we should not worry about this, but care is necessary if the velocity field is determined not analytically but numerically in a finite time interval. It is evident that an extrapolation of results to longer times is generally speaking incorrect. A hyperbolic structure in real flows, whose complexity is the reason for chaotic transport, is of a transient nature.

In conclusion, we mention chaotic transport and mixing in the atmosphere. Application of the dynamical system approach in describing transport and mixing in the atmosphere is motivated by two circumstances. Stable atmospheric stratification suppresses vertical motion. As a result, transport is mainly quasi-horizontal and occurs at isoentropic surfaces. Large-scale flows with a characteristic scale of the order of hundreds of kilometers (which is much larger than the size of clouds) are dominant. The most important passive tracers in the atmosphere are water vapor, ozone, various chemicals, and potential vorticity, which can be approximately considered a passive scalar. The rapid rotation of the Earth produces large-scale Rossby waves in the atmosphere. In two-dimensional and incompressible atmospheric flows, it is possible to introduce a streamfunction and obtain Hamiltonian equations of motion for passive particles of type (5). Using the same methods that have been applied to oceanic flows in this review, one can study manifestations of dynamical chaos in specific atmospheric models, its dynamical, statistical, and topological properties, and the fractal dynamics of transport in the atmosphere. Results of laboratory modeling of transport by Rossby waves were presented in Section 6. In references [116 – 120], mathematical aspects of transport and mixing of passive particles in running waves were studied. Some of the models considered in the cited papers had been developed in earlier papers on Hamiltonian chaos with particles in the field of two or more waves (see books [7, 121] and the references therein). Numerical simulation of chaotic advection in the atmosphere has revealed inhomogeneous mixing, barriers to transport, and anomalous transport [122 – 126] that are typical of Hamiltonian geophysical flows. Similar features have been found in the real atmosphere. For example, the boundary of the winter polar vortex in the stratosphere (the atmospheric zone ranging from 10 to 50 km) is apparently a barely permeable barrier across which transport is difficult. At middle latitudes, there are regions of strong mixing outside the vortex and to some extent inside it. The subtropical jet is a barrier separating the upper troposphere and the lower troposphere, whereas the mixing regions are located at both sides of the jet in the directions of the poles and the equator. The dynamics of chemically or biologically active diffusive impurities are of practical interest. The important role of the chaotic invariant set in geophysical flows advecting active impurities, for example, phytoplankton in the ocean and chemical reactants in the atmosphere, should be mentioned. Such sets are kinds of dynamical catalysts of biological productivity and chemical reactions.

The authors thank M Yu Uleysky and M V Budyansky for their help in preparing some figures and A Bower and L Pratt for providing their figures. This work was supported by the Program "Mathematical Methods in Nonlinear Dynamics of the Presidium of the Russian Academy of Sciences," the Russian Foundation for Basic Research (project nos. 06-01-00198, 06-05-96032, 06-05-96080), the Federal Program "The World Ocean" of the Russian Government (the project "Complex Study of Processes, Characteristics, and Resources of the Russian Far-Eastern Seas"), and by the Presidium of the Far Eastern Division of the Russian Academy of Sciences.

References

1. Dijkstra H A *Nonlinear Physical Oceanography* (Atmospheric and Oceanographic Sci. Library, Vol. 22) (Dordrecht: Kluwer, 2000)
2. Ottino J M *The Kinematics of Mixing: Stretching, Chaos, and Transport* (Cambridge: Cambridge Univ. Press, 1989)
3. Wiggins S *Annu. Rev. Fluid Mech.* **37** 295 (2005)
4. Sarkisyan A S, Akulichev V A (Eds) *Izbrannye Trudy Professora V.F. Kozlova* (Selected Papers of Professor V.F. Kozlov) (Izhevsk: Institut Komp'yuternykh Issledovanii, 2006)
5. Dutkiewicz S, Griffa A, Olson D B *J. Geophys. Res.* **98** 16487 (1993)
6. Lichtenberg A J, Lieberman M A *Regular and Stochastic Motion* (New York: Springer-Verlag, 1983) [Translated into Russian (Moscow: Mir, 1984)]
7. Zaslavsky G M, Sagdeev R Z *Vvedenie v Nelineinuyu Fiziku: Ot Mayatnika do Turbulentnosti i Khaosa* (Introduction to Nonlinear Physics: from a Pendulum to Turbulence and Chaos) (Moscow: Nauka, 1988); see also, Sagdeev R Z, Usikov D A, Zaslavsky G M *Nonlinear Physics: from the Pendulum to Turbulence and Chaos* (Chur: Harwood Acad. Publ., 1988)
8. Zaslavsky G M *Physics of Chaos in Hamiltonian Systems* (River Edge, NJ: Imperial College Press, 1998) [Translated into Russian (Moscow: Institut Komp'yuternykh Issledovanii, 2004)]

9. Arnold V I, Kozlov V V, Neishtadt A I *Matematicheskie Aspekty Klassicheskoi i Nebesnoi Mekhaniki* (Mathematical Aspects of Classical and Celestial Mechanics) (Itogi Nauki i Tekhniki. Sovremennye Problemy Matematiki. Fundamental'nye Napravleniya, Vol. 3, Ed. R V Gamkrelidze) (Moscow: VINITI, 1985) [Translated into English (Berlin: Springer, 1993)]
10. Aref H *J. Fluid Mech.* **143** 1 (1984)
11. Aref H *Phys. Fluids* **14** 1315 (2002)
12. Arnold V I *C.R. Hebd. Seances Acad. Sci.* **261** 17 (1965)
13. Hénon M *C.R. Hebd. Seances Acad. Sci.* **262** 312 (1966)
14. Eckart C *J. Mar. Res.* **7** 265 (1948)
15. Welander P *Tellus* **7** 141 (1955)
16. Lamb H *Hydrodynamics* 6th ed. (New York: Dover Publ., 1945) [Translated into Russian (Moscow – Leningrad: OGIZ, 1947)]
17. Poincaré H *C.R. Acad. Sci. Paris* **123** 1224 (1896); *Izbrannye Trudy* (Selected Papers) Vol. 1, 2 (Moscow: Nauka, 1971)
18. Kozlov V V *Simmetrii, Topologiya i Rezonansy v Gamil'tonovoi Mekhanike* (Symmetry, Topology, and Resonances in Hamiltonian Mechanics) (Izhevsk: Izd. Udm. Gos. Univ., 1995)
19. Mel'nikov V K *Tr. Mosk. Mat. Obschestva* **12** 3 (1963) [*Trans. Moscow Math. Soc.* **12** 1 (1963)]
20. Rom-Kedar V, Leonard A, Wiggins S *J. Fluid Mech.* **214** 347 (1990)
21. MacKay R S, Meiss J D, Percival I C *Physica D* **13** 55 (1984)
22. Budyansky M V, Prants S V *Pis'ma Zh. Tekh. Fiz.* **27** (12) 51 (2001) [*Tech. Phys. Lett.* **27** 508 (2001)]
23. Budyansky M V, Uleysky M Yu, Prants S V *Zh. Eksp. Teor. Fiz.* **126** 1167 (2004) [*JETP* **99** 1018 (2004)]
24. Budyansky M V, Uleysky M Yu, Prants S V *Dokl. Ross. Akad. Nauk* **386** 686 (2002) [*Dokl. Earth Sci.* **387** 929 (2002)]
25. Budyansky M V, Prants S V, in *Nelineinye Dinamicheskie Protsessy* (*k 80-letiyu so Dnya Rozhdeniya Uno Kopvillema*) (Nonlinear Dynamical Processes (to the 80th Anniversary of Uno Kopvillem)) (Ed. S V Prants) (Vladivostok: Dal'nauka, 2004) p. 63
26. Budyansky M, Uleysky M, Prants S *Physica D* **195** 369 (2004)
27. Budyansky M V, Uleysky M Yu, Prants S V, in *Proc. Fifth EUROMECH Nonlinear Dynamics Conf.* (Ed. D H van Campen et al.) (Eindhoven: Eindhoven Univ. of Technology, 2005) p. 1489
28. Mitchell K A et al. *Chaos* **13** 880 (2003)
29. Zhurbas V M, Oh I S, Pyzhevich M L *Okeanologiya* **43** 660 (2003) [*Oceanol.* **43** 622 (2003)]
30. Sainz-Trápaga S, Sugimoto T *J. Oceanogr.* **56** 79 (2000)
31. Bower A S, Lozier M S *J. Phys. Oceanogr.* **24** 1399 (1994)
32. Bower A S, Rossby T *J. Phys. Oceanogr.* **19** 1177 (1989)
33. Osborne A R et al. *Tellus* **41A** 416 (1989)
34. Osborne A R, Caponio R *Phys. Rev. Lett.* **64** 1733 (1990)
35. Brown M G, Smith K B *J. Phys. Oceanogr.* **20** 139 (1990)
36. Meyers S D, Magnan J F, O'Brien J J *Nonlinear Proc. Geophys.* **1** (1) 45 (1994)
37. Özgökmen T M et al. *J. Phys. Oceanogr.* **31** 2691 (2001)
38. Assireu A T et al. *Physica D* **168 – 169** 397 (2002)
39. Bower A S *J. Phys. Oceanogr.* **21** 173 (1991)
40. Samelson R M *J. Phys. Oceanogr.* **22** 431 (1992)
41. Uleysky M Yu, Budyansky M V, Prants S V *Nelineinaya Dinamika* **2** (2) 165 (2006)
42. Meyers S D *J. Phys. Oceanogr.* **24** 1641 (1994)
43. Duan J, Wiggins S *J. Phys. Oceanogr.* **26** 1176 (1996)
44. Dutkiewicz S, Paldor N *J. Phys. Oceanogr.* **24** 2418 (1994)
45. Yuan G-C, Pratt L J, Jones C K R T *J. Phys. Oceanogr.* **34** 1991 (2004)
46. Yang H, Liu Z *Geophys. Res. Lett.* **21** 545 (1994)
47. Yang H *J. Phys. Oceanogr.* **26** 115 (1996)
48. Poje A C, Haller G *J. Phys. Oceanogr.* **29** 1649 (1999)
49. Yang H, Liu Z *J. Phys. Oceanogr.* **27** 1258 (1997)
50. Poplvani L M, Wisdom J *Phys. Fluids A* **2** 123 (1990)
51. Dahleh M D *Phys. Fluids A* **4** 1979 (1992)
52. Kozlov V F, Gurulev A Yu *Meteorol. Gidrolog.* (6) 70 (1994) [*Meteorol. Hydrol.* (6) 41 (1994)]
53. Kozlov V F *Izv. Ross. Akad. Nauk Ser. Fiz. Atm. Okeana* **31** 245 (1995) [*Izv. Atm. Ocean. Phys.* **31** 229 (1995)]
54. Pedlosky J *Geophysical Fluid Dynamics* 2nd ed. (New York: Springer-Verlag, 1987)
55. Tikhonov A N, Samarskii A A *Uravneniya Matematicheskoi Fiziki* (Equations of Mathematical Physics) (Moscow: Nauka, 1997) [Translated into English (New York: Dover Publ., 1990)]
56. Rhines P B, Young W R *J. Fluid Mech.* **122** 347 (1982)
57. Kozlov V F, Gurulev A Yu *Izv. Ross. Akad. Nauk Ser. Fiz. Atm. Okeana* **34** 395 (1998) [*Izv. Atm. Ocean. Phys.* **34** 353 (1998)]
58. Kozlov V F, Makarov V G *Okeanologiya* **35** 658 (1995) [*Oceanol.* **35** 601 (1995)]
59. Kozlov V F, Makarov V G *Okeanologiya* **36** 493 (1996) [*Oceanol.* **36** 453 (1996)]
60. Kozlov V F, Makarov V G *Okeanologiya* **38** 505 (1998) [*Oceanol.* **38** 456 (1998)]
61. Kozlov V F, Koshel' K V *Izv. Ross. Akad. Nauk Ser. Fiz. Atm. Okeana* **35** 137 (1999) [*Izv. Atm. Ocean. Phys.* **35** 123 (1999)]
62. Liu Z, Yang H *J. Phys. Oceanogr.* **24** 1768 (1994)
63. Berloff P S, Meacham S P *J. Mar. Res.* **55** 407 (1997)
64. Meacham S P, Berloff P S *J. Mar. Res.* **55** 523 (1997)
65. Ipatova V M, Filatov A N *Izv. Ross. Akad. Nauk Ser. Fiz. Atm. Okeana* **33** 443 (1997) [*Izv. Atm. Ocean. Phys.* **33** 407 (1997)]
66. Pierrehumbert R T, Yang H *J. Atmos. Sci.* **50** 2462 (1993)
67. Kozlov V F, Koshel' K V *Izv. Ross. Akad. Nauk Ser. Fiz. Atm. Okeana* **36** 119 (2000) [*Izv. Atm. Ocean. Phys.* **36** 109 (2000)]
68. Jones S W, Aref H *Phys. Fluids* **31** 469 (1988)
69. Pierrehumbert R T *Geophys. Astrophys. Fluid Dyn.* **58** 285 (1991)
70. Yang H *Int. J. Bifurc. Chaos* **3** 1013 (1993)
71. Hogg N G *J. Fluid Mech.* **58** 517 (1973)
72. Kozlov V F *Modeli Topograficheskikh Vikhrei v Okeane* (Models of Topographical Vortices in the Ocean) (Moscow: Nauka, 1983)
73. Zyryanov V N *Topograficheskie Vikhri v Dinamike Morskikh Techenii* (Topographical Vortices in Sea-Current Dynamics) (Moscow: Inst. Vod. Problem RAN, 1995)
74. Mullineaux L S, Mills S W *Deep-Sea Res. Pt. I* **44** 745 (1997)
75. Mikhaĭlik E V, Khanchuk A I *Dokl. Ross. Akad. Nauk* **394** 234 (2004) [*Dokl. Earth Sci.* **394** 19 (2004)]
76. Goldner D R, Chapman D C *Deep-Sea Res. Pt. I* **44** 719 (1997)
77. Deese H E, Pratt L J, Helfrich K R *J. Phys. Oceanogr.* **32** 1870 (2002)
78. Sokolovskiy M A, Zyryanov V N, Davies P A *Geophys. Astrophys. Fluid Dyn.* **88** 1 (1998)
79. Carnevale G F, Kloosterziel R C, van Heijst G J *J. Fluid Mech.* **233** 119 (1991)
80. Milne-Thomson L M *Theoretical Hydrodynamics* 4th ed. (New York: Macmillan, 1960) [Translated into Russian (Moscow: Mir, 1964)]
81. Gledzer A E *Izv. Ross. Akad. Nauk Ser. Fiz. Atm. Okeana* **35** 838 (1999) [*Izv. Atm. Ocean. Phys.* **35** 759 (1999)]
82. Wiggins S *Introduction to Applied Nonlinear Dynamical Systems and Chaos* (New York: Springer-Verlag, 1990)
83. Wiggins S *Chaotic Transport in Dynamical Systems* (New York: Springer-Verlag, 1992)
84. Kozlov V F, Koshel' K V *Izv. Ross. Akad. Nauk Ser. Fiz. Atm. Okeana* **37** 378 (2001) [*Izv. Atm. Ocean. Phys.* **37** 351 (2001)]
85. Shevchenko I I *Phys. Lett. A* **241** 53 (1998)
86. Izrailsky Yu G, Kozlov V F, Koshel' K V *Phys. Fluids* **16** 3173 (2004)
87. Krauskopf B, Osinga H *J. Comput. Phys.* **146** 404 (1998)
88. Kozlov V F, Koshel' K V, Stepanov D V *Dal'nevostochyi Mat. Zh.* **2** (2) 89 (2001)
89. Kozlov V F, Koshel' K V, Stepanov D V *Izv. Ross. Akad. Nauk Ser. Fiz. Atm. Okeana* **41** 242 (2005) [*Izv. Atm. Ocean. Phys.* **41** 217 (2005)]
90. Koshel' K V, Stepanov D V *Regul. Chaotic Dyn.* **9** (4) 439 (2004)
91. Borisov A V, Mamaev I S, Sokolovskii M A (Eds) *Fundamental'nye i Prikladnye Problemy Teorii Vikhrei* (Fundamental and Applied Problems in the Vortex Theory) (Moscow – Izhevsk: Institut Komp'yuternykh Issledovanii, 2003)
92. Rom-Kedar V, Poje A C *Phys. Fluids* **11** 2044 (1999)
93. Zaslavsky G M *Stokhastichnost' Dinamicheskikh Sistem* (Stochasticity in Dynamical Systems) (Moscow: Nauka, 1984) [Translated into English: *Chaos in Dynamic Systems* (Chur: Harwood Acad. Publ., 1985)]
94. Koshel K V, Stepanov D V *Dokl. Ross. Akad. Nauk* **407** 542 (2006) [*Dokl. Earth Sci.* **407** 455 (2006)]

95. Shevchenko I I, Mel'nikov A V *Pis'ma Zh. Eksp. Teor. Fiz.* **77** 772 (2003) [*JETP Lett.* **77** 642 (2003)]
96. Koshel' K V, Izrail'skiĭ Yu G, Stepanov D V *Dokl. Ross. Akad. Nauk* **407** 773 (2006) [*Dokl. Phys.* **51** 219 (2006)]
97. Chirikov B V *Phys. Rep.* **52** 263 (1979)
98. Sommeria J, Meyers S D, Swinney H L *Nature* **337** 58 (1989)
99. Behringer R P, Meyers S D, Swinney H L *Phys. Fluids A* **3** 1243 (1991)
100. Solomon T H, Weeks E R, Swinney H L *Phys. Rev. Lett.* **71** 3975 (1993)
101. Shlesinger M F, Zaslavsky G M, Klafter J *Nature* **363** 31 (1993)
102. Weeks E R, Urbach J S, Swinney H L *Physica D* **97** 291 (1996)
103. Hart J E *Tellus* **37A** 286 (1985)
104. Mundt M D, Hart J E, Ohlsen D R *J. Fluid Mech.* **300** 311 (1995)
105. Klein P *Fluid Dyn. Res.* **5** 235 (1990)
106. Danilov S D et al. *Chaos* **6** 297 (1996)
107. Danilov S D et al. *Izv. Ross. Akad. Nauk Ser. Fiz. Atm. Okeana* **35** 810 (1999) [*Izv. Atm. Ocean. Phys.* **35** 733 (1999)]
108. Danilov S D, Dovzhenko V A, Yakyshkin I G *Zh. Eksp. Teor. Fiz.* **118** 483 (2000) [*JETP* **91** 423 (2000)]
109. Dolzhanskiĭ F V, Krymov V A, Manin D Yu *Usp. Fiz. Nauk* **160** (7) 1 (1990) [*Sov. Phys. Usp.* **33** 495 (1990)]
110. Makarov D V et al. *Phys. Rev. E* **73** 066210 (2006)
111. Makarov D V, Uleysky M Yu, Prants S V *Chaos* **14** 79 (2004)
112. Klyatskin V I, Koshel' K V *Usp. Fiz. Nauk* **170** 771 (2000) [*Phys. Usp.* **43** 717 (2000)]
113. Klyatskin V I *Diffuziya i Klasterizatsiya Passivnoi Primesi v Sluchainykh Gidrodinamicheskikh Potokakh* (Diffusion and Clasterization of Passive Scalars in Random Hydrodynamic Flows) (Moscow: Fizmatgiz, 2005)
114. Tél T et al. *Phys. Rep.* **413** 91 (2005)
115. Kuznetsov L et al. *Physica D* **191** 81 (2004)
116. Knobloch E, Weiss J B *Phys. Rev. A* **36** 1522 (1987)
117. Weiss J B *Phys. Fluids A* **3** 1379 (1991)
118. del-Castillo-Negrete D, Morrison P J *Phys. Fluids A* **5** 948 (1993)
119. Ngan K, Shepherd T G *J. Fluid Mech.* **334** 315 (1997)
120. del-Castillo-Negrete D *Phys. Fluids* **10** 576 (1998)
121. Zaslavsky G M et al. *Slabyi Khaos i Kvaziregulyarnye Struktury* (Weak Chaos and Quasiregular Patterns) (Moscow: Nauka, 1991) [Translated into English (Cambridge: Cambridge Univ. Press, 1991)]
122. Pierrehumbert R T *Phys. Fluids A* **3** 1250 (1991)
123. Pierce R B, Fairlie T D A *J. Geophys. Res.* **98** 18589 (1993)
124. Bowman K P *J. Geophys. Res.* **98** 23013 (1993)
125. Waugh D W, Plumb R A *J. Atmos. Sci.* **51** 530 (1994)
126. Shuckburgh E, Haynes P *Phys. Fluids* **15** 3342 (2003)